AD_____

AWARD NUMBER: W81XWH-04-1-0461

TITLE: Time-Resolved and Spectroscopic Three-Dimensional Optical Breast Tomography

PRINCIPAL INVESTIGATOR: Robert R. Alfano, Ph.D.

CONTRACTING ORGANIZATION: Research Foundation of CUNY
                                                New York, New York 10019-2925

REPORT DATE: April 2006

TYPE OF REPORT: Annual

PREPARED FOR: U.S. Army Medical Research and Materiel Command
                          Fort Detrick, Maryland 21702-5012

REPORT DOCUMENTATION PAGE

Form Approved
OMB No. 0704-0188

1. REPORT DATE *(DD-MM-YYYY)* 01-04-2006	2. REPORT TYPE Annual	3. DATES COVERED *(From - To)* 1 Apr 2004 – 31 Mar 2006

4. TITLE AND SUBTITLE

Time-Resolved and Spectroscopic Three-Dimensional Optical Breast Tomography

5a. CONTRACT NUMBER

5b. GRANT NUMBER
W81XWH-04-1-0461

5c. PROGRAM ELEMENT NUMBER

6. AUTHOR(S)

Robert R. Alfano, Ph.D.

E-Mail: alfano@sci.ccny.cuny.edu

5d. PROJECT NUMBER

5e. TASK NUMBER

5f. WORK UNIT NUMBER

7. PERFORMING ORGANIZATION NAME(S) AND ADDRESS(ES)

Research Foundation of CUNY
New York, New York 10019-2925

8. PERFORMING ORGANIZATION REPORT NUMBER

9. SPONSORING / MONITORING AGENCY NAME(S) AND ADDRESS(ES)
U.S. Army Medical Research and Materiel Command
Fort Detrick, Maryland 21702-5012

10. SPONSOR/MONITOR'S ACRONYM(S)

11. SPONSOR/MONITOR'S REPORT NUMBER(S)

12. DISTRIBUTION / AVAILABILITY STATEMENT
Approved for Public Release; Distribution Unlimited

13. SUPPLEMENTARY NOTES

14. ABSTRACT

The research carried out during the current reporting period included: (a) Setting up of the near-infrared optical imaging experimental arrangements, (b) Development of an approach for optical tomographic imaging using independent component analysis (OPTICA), (c) Development of a tomographic image reconstruction approach using the "round-trip matrix approach, and, (d) Target detection and localization using the combined experimental and theoretical approaches. OPTICA is applicable for detection and localization of scattering, absorptive, and fluorescent targets and was demonstrated to provide locations of targets in model media, breast phantoms, and model breasts assembled using ex vivo human breast tissues with millimeter accuracy. The "round-trip matrix" approach could locate 6 targets embedded in a turbid medium that is 50 transport mean free path thick in simulation. These results have potential applications in obtaining accurate location of tumors within breast, as well as, in lumpectomy.

15. SUBJECT TERMS
Breast cancer, near-infrared imaging, independent component analysis, tomography, target localization

16. SECURITY CLASSIFICATION OF:			17. LIMITATION OF ABSTRACT	18. NUMBER OF PAGES	19a. NAME OF RESPONSIBLE PERSON USAMRMC
a. REPORT U	b. ABSTRACT U	c. THIS PAGE U	UU	43	19b. TELEPHONE NUMBER *(include area code)*

Standard Form 298 (Rev. 8-98)
Prescribed by ANSI Std. Z39.18

Table of Contents

4. INTRODUCTION

The goal of the proposed research, "Time-Resolved and Spectroscopic Three-Dimensional Optical Breast Tomography," is to develop a safe and affordable breast cancer detection modality that uses noninvasive near-infrared (NIR) light for imaging and diagnosing tumors in human breast with high resolution and specificity. The project involves developing (a) experimental approach for probing the specimen using NIR light and collecting two-dimensional (2-D) images, and (b) image reconstruction and target localization algorithms that make use of the experimental data for generating three-dimensional (3-D) tomographic images.

In spite of a very late start owing to the time it took for the Research Protocol to be approved (USAMRMC finalized the approval on December 21, 2004), significant progress has been made during the reporting period covered by this report.

5. BODY

The tasks performed and the progress made during the current reporting period may be broadly grouped as follows:

- Development of experimental arrangements,

- Development of an approach for optical tomographic imaging using independent component analysis (OPTICA),

- Development of a tomographic image reconstruction approach using the "round-trip matrix" (RTM) approach, and

- Target detection and localization using the combined experimental and theoretical approaches.

We provide a brief outline of our accomplishments in these areas, and refer to appended publications for detailed description where applicable.

5.1. Development of Experimental Arrangements

Three complementary experimental arrangements were set up [Technical Objective (**TO**) 1, **Task 1**] and performance tested. These include a *time-resolved transillumination imaging arrangement*, a *spectroscopic imaging arrangement*, and a *multi-source illumination and multi-detector signal acquisition arrangement*.

The experimental arrangement for *time-resolved imaging* makes use of approximately 120-fs duration, 1-kHz repetition-rate, 800-nm light pulses form a Ti-sapphire laser and amplifier system for probing the sample, and an ultrafast gated intensified camera system (UGICS) for recording 2-*D* images. The UGICS is a compact gated image intensifier unit fiber-optically coupled to a charged-coupled device (CCD) camera. It provides an electronic gate pulse whose full-width-at-half-maximum duration can be adjusted to a minimum of 80-ps, and the position of the time gate could be varied over a 20 ns range with a step size of 25 ps (or some integral multiple of it). The signal recorded by the UGICS at a particular gate position, t_i is a two-dimensional (2-*D*) image, that is, a 2-*D* intensity distribution $I(x, y, t_i)$ formed by the convolution of the transmitted light pulse with the gate pulse centered on the gate position.

The *NIR spectroscopic imaging arrangement* uses the 1200-1325 nm output of a mode-locked Cr^{4+}: forsterite laser and regenerative amplifier system to illuminate the sample. A

Fourier space gate selects out a fraction of the less scattered image-bearing photons. A camera lens collects and directs these photons to the sensing element of a 320x240 pixels InGaAs NIR area camera. The resulting 2-*D* images for different wavelengths in the 1225 – 1300 nm range are recorded and displayed on a personal computer, and stored for further analysis and processing.

The *multi-source illumination and multi-detector signal acquisition arrangement* uses both the output of the Ti:sapphire laser system mentioned above, as well as, the continuous wave (CW) 784 nm radiation from a diode laser delivered by a 200-μm optical fiber for sample illumination. Multiple source illumination is realized in practice by step scanning the sample along the horizontal (*x*) and vertical (*y*) directions across the laser beam. A camera lens collects the diffusely transmitted light on the opposite face of the sample and projects it onto the sensing element of a cooled charged couple device (CCD) camera (for steady-state measurements), or the UGICS system discussed above (for time-resolved measurements). Each illuminated pixel of the CCD camera (or, the UGICS system) could be regarded as a detector. For illumination of every scanned point on the input surface of the sample, the CCD camera (or, the UGICS system) records the diffusely transmitted intensity pattern on the output surface.

5.2. Optical Tomographic Imaging using Independent Component Analysis (OPTICA)

One of our major accomplishments during this reporting period is the development of a novel target detection and localization approach,[1-2] OPTICA that enables 3-D localization of target with high level of accuracy [**TO 3, TO 4, Task 1, Task 2, Task 6**]. The approach makes use of transmitted light signal collected by multiple detectors following multiple-source illumination of the turbid medium containing the targets. The resulting multiple angular views provide robust data that is analyzed using the independent component analysis[3] (ICA) of information theory to determine the locations of targets relative to the medium boundaries with millimeter accuracy. OPTICA also provides a cross-sectional image of the target within the turbid medium. OPTICA may be used for detection, localization and imaging of absorptive, scattering and fluorescent targets. The details of the approach were published and are attached to this document as *Appendices* 1,2,4,5.

5.3. Optical Tomography using 'round-trip matrix'

We have developed a new numerical algorithm [**TO 3, Task 6**] for obtaining tomographic images of targets in turbid medium, and tested it using simulated data.[4] In this approach, the transport of light from multiple sources through the turbid medium to an array of detectors is represented by a response matrix that can be constructed from experimental data. The 'round-trip matrix' (RTM) is constructed by multiplying the response matrix by its transpose for CW (adjoint matrix for frequency-modulated and short-pulse) illumination. The RTM provides a mathematical description of transport of light from the sources through the turbid medium with embedded objects to the array of detectors and back, and is similar to the time-reversal matrix used in the general area of array processing for acoustic and radar imaging. The vector subspace method along with Green's function calculated from an appropriate forward model is then used to detect the targets. In test runs using simulated data,[4] the approach was able to locate 6 targets at different locations within a turbid medium of thickness $50l_t$ (l_t = transport mean free path of the medium) (detailed in Reference 4 attached as *Appendix* 3). While the simulated data used slab geometry, the approach can be used for other sample geometries and to different forward models.

5.4. Target Detection, Localization and Imaging

We have used the experimental data (obtained using the experimental arrangements outlined in Section 5.1) along with the OPTICA algorithms (Section 5.2) on different types of samples to obtain target location and cross sectional images (*Appendices 2,4 and 5*), and demonstrated potential of both OPTICA (*Appendix 1*) and RTM (*Appendix 3*) approaches using simulated data.

The samples included Intralipid-10% suspension in water (concentration adjusted to mimic the scattering coefficient, absorption coefficient, and anisotropy factor of human breast tissue), breast phantom obtained from Professor Hebden's Group at University College London (UCL),[5] a small piece of porcine liver embedded in porcine tissue, and what is most important realistic breast models formed using *ex vivo* breast tissues obtained from National Disease Research Interchange (NDRI) [along the line of **TO 1, Task 2**].

We have initiated measurements using light of different wavelengths [**TO 2, Task 4**] to obtain estimates of scattering coefficient, absorption coefficient, and anisotropy factor of breast tissue specimens. Details of the results are presented in the appended publications, and key results are mentioned in the following "*Key Research Accomplishments*" Section.

6. KEY RESEARCH ACCOMPLISHMENTS

- Developed the Optical Tomography using Independent Component Analysis (OPTICA) approach for detection, 3-D localization, and cross section imaging of targets embedded in a turbid medium (*Appendices 1, 2, 4,5*).

- Demonstrated the efficacy of OPTICA in detecting and locating scattering, absorptive, and fluorescent targets. Key results include:

    (i)   Detection and localization of 4 small scattering targets in a breast phantom (UCL sample, Reference 5), the weakest one having a scattering coefficient of only 1.1 times that of the intervening media (and was considered to be "rather unlikely to be found"[5] within mm accuracy (detailed in *Appendix 2*);

    (ii)   Detection of two absorptive targets in a breast tissue-simulating model medium of thickness 50 times the transport mean free path (l_t) (detailed in *Appendix 5*);

    (iii)   Detection of a 4-mm diameter fluorescent sphere in a breast tissue-simulating model medium of thickness 50 times the transport mean free path (l_t) (detailed in *Appendix 4*).

- Detection and localization of a small tumor (~ 5 mm x 5 mm x 3 mm) in a breast model (42 mm x 30 mm x 33 mm) assembled using *ex vivo* breast tissues.

- Developed a new "round-trip matrix" algorithm for obtaining tomographic images of targets in turbid medium, and tested it using simulated data. The approach could locate all 6 targets when simulated data was used (detailed in *Appendix 3*).

7. REPORTABLE OUTCOMES

Journal Articles

1. M. Xu, M. Alrubaiee, S. K. Gayen and R. R. Alfano, "Three-dimensional optical imaging of objects in a turbid medium using independent component analysis: theory and simulation," *J. Biomed. Opt.* **10**, 051705 (2005).

2. M. Alrubaiee, M. Xu, S. K. Gayen, M. Brito, and R. R. Alfano, "Three-dimensional optical tomographic imaging of objects in tissue-simulating turbid medium using independent component analysis," *Appl. Phys. Lett.* **87**, 191112 (2005).

Conference Proceedings

3. W. Cai, M. Alrubaiee, S. K. Gayen, M. Xu, and R. R. Alfano, "Three-dimensional optical tomography of objects in turbid media using the 'round-trip matrix," in Optical Tomography and Spectroscopy of Tissue VI, edited by Britton Chance, Robert R. Alfano, Bruce J. Tromberg, Mamoru Tamura, Eva M. Sevick-Muraca, Proceedings of SPIE, Vol. 5693 (SPIE, Bellingham, WA, 2005), pp. 4-9.

4. M. Alrubaiee, M. Xu, S. K. Gayen, and R. R. Alfano, "Fluorescence optical tomography using independent component analysis to detect small objects in turbid media," in Optical Tomography and Spectroscopy of Tissue VI, edited by Britton Chance, Robert R. Alfano, Bruce J. Tromberg, Mamoru Tamura, Eva M. Sevick-Muraca, Proceedings of SPIE Vol. 5693 (SPIE, Bellingham, WA, 2005), pp. 221-224.

5. M. Xu, M. Alrubaiee, S. K. Gayen, and R. R. Alfano, "Optical tomography using independent component analysis to detect absorptive, scattering, or fluorescent inhomogeneities in turbid media," in *Optical Tomography and Spectroscopy of Tissue VI,* edited by Britton Chance, Robert R. Alfano, Bruce J. Tromberg, Mamoru Tamura, Eva M. Sevick-Muraca, Proceedings of SPIE Vol. 5693 (SPIE, Bellingham, WA, 2005), pp. 528 – 535.

Presentations

1. M. Xu, M. Alrubaiee, W. Cai, S. K. Gayen, and R. R. Alfano, "Toward optical imaging of small tumors in breasts using cumulant forward model and Independent Component Analysis," Paper P14-19 presented at the Era of Hope, Department of Defense Breast Cancer Research Program Meeting, June 8-11, 2005, Philadelphia, PA.

2. M. Alrubaiee, M. Xu, S. K. Gayen, and R. R. Alfano, "Optical tomography using Independent Component Analysis for breast cancer detection," Paper P64-2 presented at the Era of Hope, Department of Defense Breast Cancer Research Program Meeting, June 8-11, 2005, Philadelphia, PA.

3. M. Alrubaiee, M. Xu, S. K. Gayen, and R. R. Alfano, "Three-dimensional localization of scattering targets in turbid media using Independent Component Analysis," Paper CThJ3 presented at the Conference on Lasers and Electro-Optics (CLEO), May 22-27, 2005, Baltimore, Maryland.

4. M. Xu, M. Alrubaiee, S. K. Gayen, and R. R. Alfano, "Fluorescence optical imaging in turbid media using Independent Component Analysis," Paper CFJ1 presented at the

Conference on Lasers and Electro-Optics (CLEO), May 22-27, 2005, Baltimore, Maryland.

5. W. Cai, M. Alrubaiee, S. K. Gayen, M. Xu, and R. R. Alfano, "Three-dimensional optical tomography of objects in turbid media using the 'round-trip matrix." Paper 5693-02 presented at the Optical Tomography and Spectroscopy of Tissue VII Conference of SPIE's BiOS 2005/ Photonics West, January 22-27, 2005, San Jose, California.

6. M. Alrubaiee, M. Xu, S. K. Gayen, and R. R. Alfano, "Fluorescence optical tomography using independent component analysis to detect small objects in turbid media." Paper 5693-39 presented at the Optical Tomography and Spectroscopy of Tissue VII Conference of SPIE's BiOS 2005/ Photonics West, January 22-27, 2005, San Jose, California.

7. M. Xu, M. Alrubaiee, S. K. Gayen, and R. R. Alfano, "Optical tomography using independent component analysis to detect absorptive, scattering, or fluorescent inhomogeneities in turbid media." Paper 5693-02 presented at the Optical Tomography and Spectroscopy of Tissue VII Conference of SPIE's BiOS 2005/ Photonics West, January 22-27, 2005, San Jose, California.

8. CONCLUSION

The work carried out during this reporting period shows the potential for detection and three-dimensional localization of targets (including tumor) within a turbid medium (including a model breast formed with *ex vivo* tissues) with significant accuracy based on the differences in the scattering, absorption, and fluorescence characteristics of the target (*e.g.,* tumor) and the intervening medium (*e.g.,* normal breast tissue).

   "*So What Section*"

- A recent study involving 35,319 patients underscores the influence of primary tumor location on breast cancer prognosis, and makes it imperative that breast cancer detection modalities obtain three dimensional (3-D) location of the tumor relative to the axilla.[6] The current work is an important development in obtaining noninvasive 3-D location of a tumor within the breast.

- The applicability of OPTICA for scattering, absorptive, and fluorescent targets makes it versatile since all three phenomena may be used for contrast enhancement between the tumor and normal breast tissues. Fluorescence-based detection may require use of contrast agents, such as, molecular beacons. Use of far-red and NIR native fluorescence wing[7] is also a possibility.

- Three-dimensional target localization will enable closer probing of a smaller volume around of the target providing more details since smaller pixel size could be used without increasing the computation time (as a smaller volume will be probed).

- Further development of the OPTICA approach may find another important application in lumpectomy, where the surgeon looks for the margins of the tumor with high accuracy.

9. REFERENCES

1. M. Xu, M. Alrubaiee, S. K. Gayen and R. R. Alfano, "Three-dimensional optical imaging of objects in a turbid medium using independent component analysis: theory and simulation," *J. Biomed. Opt.* **10**, 051705 (2005).

2. M. Alrubaiee, M. Xu, S. K. Gayen, M. Brito, and R. R. Alfano, "Three-dimensional optical tomographic imaging of objects in tissue-simulating turbid medium using independent component analysis," *Appl. Phys. Lett.* **87**, 191112 (2005).

3. P. Comon, "Independent component analysis – a new concept?" *Signal Process.* **36**, 287 (1994).

4. W. Cai, M. Alrubaiee, S. K. Gayen, M. Xu, and R. R. Alfano, "Three-dimensional optical tomography of objects in turbid media using the 'round-trip matrix," in Optical Tomography and Spectroscopy of Tissue VI, edited by Britton Chance, Robert R. Alfano, Bruce J. Tromberg, Mamoru Tamura, Eva M. Sevick-Muraca, Proceedings of SPIE, Vol. 5693 (SPIE, Bellingham, WA, 2005), pp. 4-9.

5. D. J. Hall, J. C. Hebden, and D. T. Deply, "Imaging very low contrast objects in breastlike scattering media with a time-resolved method," *Appl. Opt.* **36**, 7270 – 7276 (1997).

6. N. Kroman, J. Wohlfahrt, H. T. Mouridsen, and M. Melbye, "Influence of tumor location on breast cancer prognosis," *Int. J. Cancer* **105**, 542 -545 (2003).

7. G. Zhang, S. G. Demos, R. R. Alfano, "Far-red and NIR spectral wing emission from tissues under 532 and 632 nm photo excitation," *Lasers Life Sci.* **9**, 1-16 (1999).

10. APPENDICES

Appendix 1.   M. Xu, M. Alrubaiee, S. K. Gayen and R. R. Alfano, "Three-dimensional optical imaging of objects in a turbid medium using independent component analysis: theory and simulation," *J. Biomed. Opt.* **10**, 051705 (2005).

Appendix 2.   M. Alrubaiee, M. Xu, S. K. Gayen, M. Brito, and R. R. Alfano, "Three-dimensional optical tomographic imaging of objects in tissue-simulating turbid medium using independent component analysis," *Appl. Phys. Lett.* **87**, 191112 (2005).

Appendix 3.   W. Cai, M. Alrubaiee, S. K. Gayen, M. Xu, and R. R. Alfano, "Three-dimensional optical tomography of objects in turbid media using the 'round-trip matrix'," in Optical Tomography and Spectroscopy of Tissue VI, edited by Britton Chance, Robert R. Alfano, Bruce J. Tromberg, Mamoru Tamura, Eva M. Sevick-Muraca, Proceedings of SPIE, Vol. 5693 (SPIE, Bellingham, WA, 2005), pp. 4-9.

Appendix 4.   M. Alrubaiee, M. Xu, S. K. Gayen, and R. R. Alfano, "Fluorescence optical tomography using independent component analysis to detect small objects in turbid media," in Optical Tomography and Spectroscopy of Tissue VI, edited by Britton Chance, Robert R. Alfano, Bruce J. Tromberg, Mamoru Tamura, Eva M. Sevick-Muraca, Proceedings of SPIE Vol. 5693 (SPIE, Bellingham, WA, 2005), pp. 221-224.

Appendix 5.   M. Xu, M. Alrubaiee, S. K. Gayen, and R. R. Alfano, "Optical tomography using independent component analysis to detect absorptive, scattering, or fluorescent inhomogeneities in turbid media," in *Optical Tomography and Spectroscopy of Tissue VI,* edited by Britton Chance, Robert R. Alfano, Bruce J. Tromberg, Mamoru Tamura, Eva M. Sevick-Muraca, Proceedings of SPIE Vol. 5693 (SPIE, Bellingham, WA, 2005), pp. 528 – 535.

Optical imaging of turbid media using independent component analysis: theory and simulation

M. Xu
M. Alrubaiee
S. K. Gayen
R. R. Alfano
The City College and Graduate Center of the City
    University of New York
Department of Physics
Institute for Ultrafast Spectroscopy and Lasers
New York, New York 10031

Abstract. A new imaging approach for 3-D localization and characterization of objects in a turbid medium using independent component analysis (ICA) from information theory is developed and demonstrated using simulated data. This approach uses a multisource and multidetector signal acquisition scheme. ICA of the perturbations in the spatial intensity distribution measured on the medium boundary sorts out the embedded objects. The locations and optical characteristics of the embedded objects are obtained from a Green's function analysis based on any appropriate model for light propagation in the background medium. This approach is shown to locate and characterize absorptive and scattering inhomogeneities within highly scattering medium to a high degree of accuracy. In particular, we show this approach can discriminate between absorptive and scattering inhomogeneities, and can locate and characterize complex inhomogeneities, which are both absorptive and scattering. The influence of noise and uncertainty in background absorption or scattering on the performance of this approach is investigated. © *2005 Society of Photo-Optical Instrumentation Engineers.* [DOI: 10.1117/1.2101568]

Keywords: image processing; image reconstruction; medical imaging; inverse problems; absorption; scattering; diffusion; radiative transfer.

1 Introduction

Optical probing of the interior of multiply scattering colloidal suspensions and biological materials has attracted much attention over the last decade. In particular, biomedical optical tomography and spectroscopy, which has the potential to provide functional information about brain activities and diagnostic information about tumors in breast and prostate, are being actively pursued.[1–17] Simultaneous developments in experimental apparatus and techniques for object interrogation and signal acquisition,[2,4,5,18,19] analytical models for light propagation,[10,20–22] and computer algorithms for image reconstruction[6,8] hold promise for realization of these potentials of optical tomography.

Multiple scattering of light in thick turbid media precludes direct imaging of embedded targets. One typically uses an inverse image reconstruction[6,8] (IIR) approach to reconstruct a map of the optical properties, such as absorption coefficient (μ_a) and scattering coefficient (μ_s), of the medium by matching the measured light intensity distribution on the boundary of the turbid medium to that calculated by a forward model for the propagation of light in that medium. The commonly used forward models include the radiative transfer equation[17,23] (RTE), the diffusion approximation (DA) of the RTE (Refs. 6 and 8), and random walk of photons.[24,25]

The inversion problem is ill-posed and must be regularized to stabilize the inversion at a cost of reduced resolution.[8,26] Both iterative reconstruction and noniterative linearized inversion approaches have been used to solve the inversion problem in optical tomography, which is weakly nonlinear, with limited success. Reconstruction of images with adequate spatial resolution and accurate localization and characterization of the inhomogeneities remain a formidable task. The time required for data acquisition and image reconstruction is another important consideration.

In this paper, we present a novel algorithm based on the independent component analysis[27,28] (ICA) from information theory to locate absorptive and scattering inhomogeneities embedded in a thick turbid medium and demonstrate the efficacy using simulated data. ICA has been successfully applied in various other applications such as electroencephalogram and nuclear magnetic resonance spectroscopy.[28–31] We refer to this information theory-inspired approach as optical imaging using independent component analysis, abbreviated as, OPTICA. The novelty of OPTICA over other ICA applications is that OPTICA associates directly the independent components to the Green's functions responsible for light propagation in the turbid medium from the inhomogeneities to the source and the detector, and therefore the retrieved independent components can be used to locate and characterize the inhomogeneities.

OPTICA uses a multisource illumination and multidetector signal acquisition scheme providing a variety of spatial and

Address all correspondence to M. Xu, the City College of the City University of New York, Department of Physics, J419, 138th Street and Convent Avenue, New York, New York 10031. Tel.: (212) 650-6865; Fax: (212) 650-5530; E-mail: minxu@sci.ccny.cuny.edu

angular views essential for three-dimensional (3-D) object localization. Each object (or inhomogeneity) within the turbid medium alters the propagation of light through the medium. The influence of an object on the spatial distribution of the light intensity at the detector plane involves propagation of light from the source to the object, and from the object to the detector, and can be described in terms of two Green's functions (propagators) describing light propagation from source to the object and that from the object to the detector, respectively.

The absorptive or scattering inhomogeneities illuminated by the incident wave are assumed to be virtual sources, and the perturbation of the spatial distribution of the light intensity on the medium boundary is taken to be some weighted mixture of signals arriving from these virtual sources. These virtual sources are statistically independent and can be recovered by ICA of the recorded data set. The number of leading independent components is same as the number of embedded objects. The location and characterization of inhomogeneities are obtained from the analysis of the retrieved virtual sources using an appropriate model of light propagation in the background medium.

The remainder of this paper is organized as follows. Section 2 presents a brief introduction to ICA and reviews the general theoretical framework for OPTICA. Section 3 presents the results from simulations for different configurations. Implications of these results are discussed in Sec. 4.

2 Theoretical Formalism

2.1 ICA

Blind source separation is a class of problem of general interest that consists of recovering unobserved signals or virtual sources from several observed mixtures. Typically the observations are the output of a set of sensors, where each sensor receives a different combination of the source signals. Prior knowledge about the mixture in such problems is usually not available. The lack of prior knowledge is compensated by a statistically strong but often physically plausible assumption of independence between the source signals. Over the last decade, ICA has been proposed as a solution to the blind source separation problem and has emerged as a new paradigm in signal processing and data analysis.[27,28,31,32]

The simplest ICA model, an instantaneous linear mixture model,[32] assumes the existence of n independent signals $s_i(t)$ $(i=1,2,\dots,n)$ and the observation of at least as many mixtures $x_i(t)$ $(i=1,2,\dots,m)$ by $m \geq n$ sensors, these mixtures being linear and instantaneous, i.e., $x_i(t)=\sum_{j=1}^{n} a_{ij} s_j(t)$ for each i at a sequence of time t. In a matrix notation,

$$\mathbf{x}(t) = \mathbf{A}\mathbf{s}(t), \quad \mathbf{A} \in \mathbb{R}^{m \times n}, \tag{1}$$

where $\mathbf{A}$ is the mixing matrix. The j'th column of $\mathbf{A}$ gives the mixing vector for the j'th virtual source. ICA can be formulated as the computation of an $n \times m$ separating matrix $\mathbf{B}$ whose output

$$\mathbf{y}(t) = \mathbf{B}\mathbf{x}(t) = \mathbf{C}\mathbf{s}(t), \quad \mathbf{B} \in \mathbb{R}^{n \times m}, \quad \mathbf{C} \equiv \mathbf{B}\mathbf{A} \in \mathbb{R}^{n \times n},$$

$$\tag{2}$$

is an estimate of the vector $\mathbf{s}(t)$ of the source signals.

The basic principle of ICA can be understood in the following way. The central limit theorem in probability theory tells us that the distribution of independent random variables tends toward a Gaussian distribution under certain conditions. Thus, a sum of multiple independent random variables usually has a distribution that is closer to Gaussian than any of the original random variables. In Eq. (2) $y_i(t) = \sum_j C_{ij} s_j(t)$, as a summation of independent random variables $s_j(t)$, is usually more Gaussian than $s_j(t)$, while $y_i(t)$ becomes least Gaussian when it in fact equals one of the $s_j(t)$. This heuristic argument shows that ICA can be intuitively regarded as a statistical approach to find the separating matrix $\mathbf{B}$ such that $y_i(t)$ is least Gaussian. This can be achieved by maximizing some measure of non-Gaussianity, such as maximizing kurtosis[32,33] (the fourth-order cumulate), of $y_i(t)$.

ICA separates independent sources from linear instantaneous or convolutive mixtures of independent signals without relying on any specific knowledge of the sources except that they are independent. The sources are recovered by a maximization of a measure of independence (or, a minimization of a measure of dependence), such as non-Gaussianity and mutual information between the reconstructed sources.[31,32] The recovered virtual sources and mixing vectors from ICA are unique up to permutation and scaling.[31,32]

2.2 Optical Imaging Using ICA

The classical approach to propagation of multiply scattered light in turbid media, which assumes that phases are uncorrelated on scales larger than the scattering mean free path l_s, leads to the RTE in which any interference effects are neglected.[34] The RTE does not admit closed-form analytical solutions in bounded regions and its numerical solution is computationally expensive. The commonly used forward models in optical imaging of highly scattering media is[6,8] the DA to RTE.

The approach OPTICA can be applied to different models of light propagation in turbid media, such as the diffusion approximation,[6,8] the cumulant approximation,[20,22,35] the random walk model,[10,24] and radiative transfer[17,34] when they are linearized. The diffusion approximation is valid when the inhomogeneities are deep within a highly scattering medium. We discuss only the formalism of OPTICA in the diffusion approximation in this paper.

In this diffusion approximation, the perturbation of the detected light intensities on the boundaries of the medium, the scattered wave field, due to absorptive and scattering objects (inhomogeneities) can be written as[3,13]

$$\phi_{\mathrm{sca}}(\mathbf{r}_d, \mathbf{r}_s) = -\int G(\mathbf{r}_d, \mathbf{r}) \delta\mu_a(\mathbf{r}) c G(\mathbf{r}, \mathbf{r}_s) d\mathbf{r}$$

$$- \int \delta D(\mathbf{r}) c \nabla_{\mathbf{r}} G(\mathbf{r}_d, \mathbf{r}) \cdot \nabla_{\mathbf{r}} G(\mathbf{r}, \mathbf{r}_s) d\mathbf{r}, \tag{3}$$

to the first order of the Born approximation[36] when illuminated by a point source of unit power, where $\mathbf{r}_s$, $\mathbf{r}$, and $\mathbf{r}_d$ are the positions of the source, the inhomogeneity, and the detector, respectively; $\delta\mu_a = \mu_{a,\mathrm{obj}} - \mu_a$ and $\delta D = D_{\mathrm{obj}} - D$ are the differences in absorption coefficient and diffusion coefficient, respectively, between the inhomogeneity and the background;

c is the speed of light in the medium; and $G(\mathbf{r},\mathbf{r}')$ is the Green's function describing light propagation from $\mathbf{r}'$ to $\mathbf{r}$ inside the background turbid medium of absorption and diffusion coefficients μ_a and D.

Equation (3) is written in the frequency domain and does not explicitly show the modulation frequency ω of the incident wave for clarity. The following formalism applies to continuous wave, frequency-domain, and time-resolved measurements. The time-domain measurement is first Fourier transformed over time to obtain data over many different frequencies.

The Green's function G for a slab geometry in DA is given by

$$G(\mathbf{r},\mathbf{r}') \equiv G(\rho,z,z') = \frac{1}{4\pi D} \sum_{k=-\infty}^{\infty} \left[\frac{\exp(-\kappa r_k^+)}{r_k^+} - \frac{\exp(-\kappa r_k^-)}{r_k^-} \right]$$

$$r_k^\pm = [\rho^2 + (z \mp z' \pm 2kd)^2]^{1/2}, \qquad (4)$$

for an incident amplitude-modulated wave of modulation frequency ω, where $k = 0, \pm 1, \pm 2, \dots, \rho = [(x-x')^2 + (y-y')^2]^{1/2}$ is the distance between the two points $\mathbf{r} = (x,y,z)$ and $\mathbf{r}' = (x',y',z')$ projected onto the xy plane; $\kappa = [(\mu_a - i\omega/c)/D]^{1/2}$ is chosen to have a nonnegative real part; and the extrapolated boundaries of the slab are located at $z=0$ and $z=d=L_z+2z_e$, respectively, where L_z is the physical thickness of the slab and the extrapolation length z_e should be determined from the boundary condition of the slab.[37–39] Greens' functions in Eq. (3) for other geometries can be obtained either analytically or numerically.[40,41]

2.2.1 Absorptive inhomogeneities

We first consider absorptive inhomogeneities. Under the assumption that absorptive inhomogeneities are localized, that is, the j'th one is contained in volume V_j centered at $\mathbf{r}_j (1 \leqslant j \leqslant J)$, the scattered wave field in Eq. (3) can be rewritten as

$$-\phi_{\text{sca}}(\mathbf{r}_d,\mathbf{r}_s) = \sum_{j=1}^{J} G(\mathbf{r}_d,\mathbf{r}_j) q_j G(\mathbf{r}_j,\mathbf{r}_s), \qquad (5)$$

where $q_j = \delta\mu_a(\mathbf{r}_j) c V_j$ is the absorption strength of the j'th inhomogeneity. The scattered wave is in a form of an instantaneous linear mixture of Eq. (1). One absorptive inhomogeneity is represented by one virtual source $q_j G(\mathbf{r}_j,\mathbf{r}_s)$ with a mixing vector $G(\mathbf{r}_d,\mathbf{r}_j)$.

As the virtual source $q_j G(\mathbf{r}_j,\mathbf{r}_s)$ at the j'th inhomogeneity is independent of the virtual sources at other locations, ICA can be used with the observations obtained for the light source at $n \gg J$ different positions to separate out both virtual sources $s_j(\mathbf{r}_s)$ and the mixing vectors[27,32] $a_j(\mathbf{r}_d)$. The j'th virtual source $s_j(\mathbf{r}_s)$ and the j'th mixing vector $a_j(\mathbf{r}_d)$ provide the scaled projections of the Green's function on the source and detector planes, $G(\mathbf{r}_j,\mathbf{r}_s)$ and $G(\mathbf{r}_d,\mathbf{r}_j)$, respectively. We can write

$$s_j(\mathbf{r}_s) = \alpha_j G(\mathbf{r}_j,\mathbf{r}_s),$$

$$a_j(\mathbf{r}_d) = \beta_j G(\mathbf{r}_d,\mathbf{r}_j), \qquad (6)$$

where α_j and β_j are scaling constants for the j'th inhomogeneity.

Both the location and strength of the j'th object can be computed by a simple fitting procedure using Eq. (6). We adopted a least-squares fitting procedure given by:

$$\min_{\mathbf{r}_j,\alpha_j,\beta_j} \left\{ \sum_{\mathbf{r}_s} [\alpha_j^{-1} s_j(\mathbf{r}_s) - G(\mathbf{r}_j,\mathbf{r}_s)]^2 + \sum_{\mathbf{r}_d} [\beta_j^{-1} a_j(\mathbf{r}_d) - G(\mathbf{r}_d,\mathbf{r}_j)]^2 \right\}. \qquad (7)$$

The fitting yields the location $\mathbf{r}_j$ and the two scaling constants α_j and β_j for the j'th inhomogeneity whose absorption strength is then given by $q_j = \alpha_j\beta_j$.

2.2.2 Scattering inhomogeneities

For scattering inhomogeneities, a similar analysis shows the scattered wave can be written as

$$-\phi_{\text{sca}}(\mathbf{r}_d,\mathbf{r}_s) = \sum_{j=1}^{J'} g_z(\mathbf{r}_j,\mathbf{r}_d) q_j' g_z(\mathbf{r}_j,\mathbf{r}_s)$$

$$+ \sum_{j=1}^{J'} \rho_{dj} \cos\theta_d g_\perp(\mathbf{r}_j,\mathbf{r}_d) q_j' \rho_{sj} \cos\theta_s g_\perp(\mathbf{r}_j,\mathbf{r}_s)$$

$$+ \sum_{j=1}^{J'} \rho_{dj} \sin\theta_d g_\perp(\mathbf{r}_j,\mathbf{r}_d) q_j' \rho_{sj} \sin\theta_s g_\perp(\mathbf{r}_j,\mathbf{r}_s), \qquad (8)$$

where $q_j' = \delta D(\mathbf{r}_j) c V_j'$ is the diffusion strength of the j'th scattering inhomogeneity of volume V_j' $(j=1,2,\dots,J')$; $\rho_{dj} = [(x_d-x_j)^2 + (y_d-y_j)^2]^{1/2}$, $\rho_{sj} = [(x_s-x_j)^2 + (y_s-y_j)^2]^{1/2}$; θ_d and θ_s are the azimuthal angles of $\mathbf{r}_d - \mathbf{r}_j$ and $\mathbf{r}_s - \mathbf{r}_j$, respectively, and the two auxiliary functions are given by

$$g_\perp(\mathbf{r},\mathbf{r}') = \frac{1}{4\pi D} \sum_{k=-\infty}^{+\infty} \left[(\kappa r_k^+ + 1)\frac{\exp(-\kappa r_k^+)}{(r_k^+)^3} - (\kappa r_k^- + 1)\frac{\exp(-\kappa r_k^-)}{(r_k^-)^3} \right], \qquad (9)$$

and

$$g_z(\mathbf{r},\mathbf{r}') = \frac{1}{4\pi D} \sum_{k=-\infty}^{+\infty} \left\{ (z - z' + 2kd)(\kappa r_k^+ + 1)\frac{\exp(-\kappa r_k^+)}{(r_k^+)^3} - (z + z' - 2kd)(\kappa r_k^- + 1)\frac{\exp(-\kappa r_k^-)}{(r_k^-)^3} \right\}. \qquad (10)$$

The scattered wave from one scattering inhomogeneity is thus a mixture of contributions from $(3J')$ virtual sources:

$$q_j' g_z(\mathbf{r}_j,\mathbf{r}_s), \quad q_j' \rho_{sj} \cos\theta_s g_\perp(\mathbf{r}_j,\mathbf{r}_s), \quad q_j' \rho_{sj} \sin\theta_s g_\perp(\mathbf{r}_j,\mathbf{r}_s), \qquad (11)$$
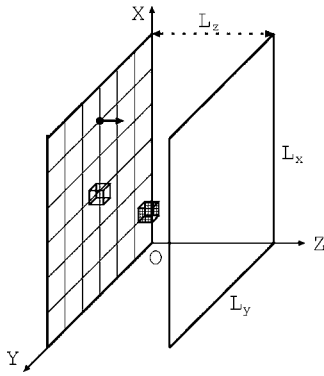
with mixing vectors

Fig. 1 Light intensity on one side of the slab is measured when a point source scans on the other side. Two inhomogeneities are placed at (50, 60, 20) and (30, 30, 30) mm inside the slab.

$$g_z(\mathbf{r}_j,\mathbf{r}_d), \quad \rho_{dj}\cos\theta_d g_\perp(\mathbf{r}_j,\mathbf{r}_d), \quad \rho_{dj}\sin\theta_d g_\perp(\mathbf{r}_j,\mathbf{r}_d),$$

$$(12)$$

where $1 \leqslant j \leqslant J'$, respectively. Both the location and strength of the j'th scattering object are computed by fitting the retrieved virtual sources and mixing vectors to Eqs. (11) and (12) using a least-squares procedure, respectively.

There are, in general, three virtual sources of specific patterns (one centrosymmetric and two dumbbell-shaped) associated with one scattering inhomogeneity, whereas only one centrosymmetric virtual source is associated with one absorptive inhomogeneity. This difference may serve as the basis to discriminate absorptive and scattering inhomogeneities.

The only assumption made in OPTICA is that virtual sources are mutually independent. The number of inhomogeneities within the medium is determined by the number of the independent components presented in the multisource multidetector data set. No specific light propagation model is assumed in this step. The analysis of retrieved independent components from ICA then localizes and characterizes the absorptive and scattering inhomogeneities inside the turbid medium using an appropriate model of the light propagator. Extra independent components may appear, depending on the level of noise in the data. These components can be discarded and only the leading independent components must be analyzed to detect and characterize inhomogeneities of interest.

3 Results

Simulations were performed for a 50-mm-thick slab, as shown schematically in Fig. 1. The absorption and diffusion coefficients of the uniform slab are $\mu_a = 1/300$ mm^{-1} and $D = 1/3$ mm, respectively, close to that of human breast tissue.[42] The incident cw beam scans a set of 21×21 grid points covering an area of 90×90 mm^2. The spacing between two consecutive grid points is 4.5 mm. This light intensity on the other side of the slab is recorded by a CCD camera on 42×42 grid points covering the same area.

In the simulations presented in the following subsections, we fix the ratio of strength of absorption to that of diffusion to be 0.01, which produce perturbations of comparable magnitude on the light intensities measured on the detector plane from the absorption and scattering inhomogeneities. As the
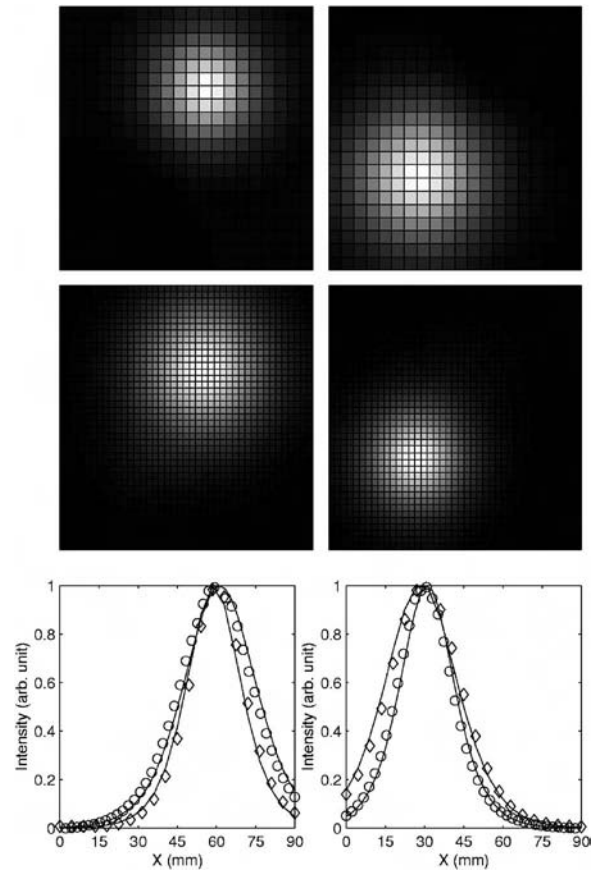

Fig. 2 Normalized independent spatial intensity distributions on the input (or source) plane (the first row), the exit (or detector) plane (the second row), and the least-squares fitting using Eq. (7) (the third row). The left column is for the first absorptive inhomogeneity at (50, 60, 20) mm and the right column is for the second absorptive inhomogeneity at (30, 30, 30) mm. On the third row, the horizontal profile of intensity distributions on the source plane (diamonds) and on the detector plane (circles) are displayed, and solid lines show the respective Green's function fit used for obtaining locations and strengths of objects. The noise level is 5%.

scattered wave is linear with respect to the absorption and diffusion strengths, we also set the strength of either absorption or diffusion to be unity in simulations for convenience.

3.1 Absorptive Inhomogeneities

Two absorptive inhomogeneities, each of a unity absorption strength, are placed at positions (50, 60, 20) and (30, 30, 30) mm, respectively. Gaussian noise of 5% was added to the simulated light intensity change on the detector plane. OPTICA operates on a noisy scattering wave $-\phi_{\text{sca}}(\mathbf{r}_d,\mathbf{r}_s)[1+n(\mathbf{r}_d,\mathbf{r}_s)]$, where $n(\mathbf{r}_d,\mathbf{r}_s)$ is a Gaussian random variable of a standard deviation 0.05.

ICA of the perturbations in the spatial intensity distributions provided corresponding independent intensity distributions on the source and detector planes. ICA-generated independent intensity distributions on the source and detector planes are shown in Fig. 2 for the two absorptive inhomogeneities. Locations of the absorptive objects are obtained from fitting these independent component intensity distributions to those of the diffusion approximation in a slab Eq. (4) by the
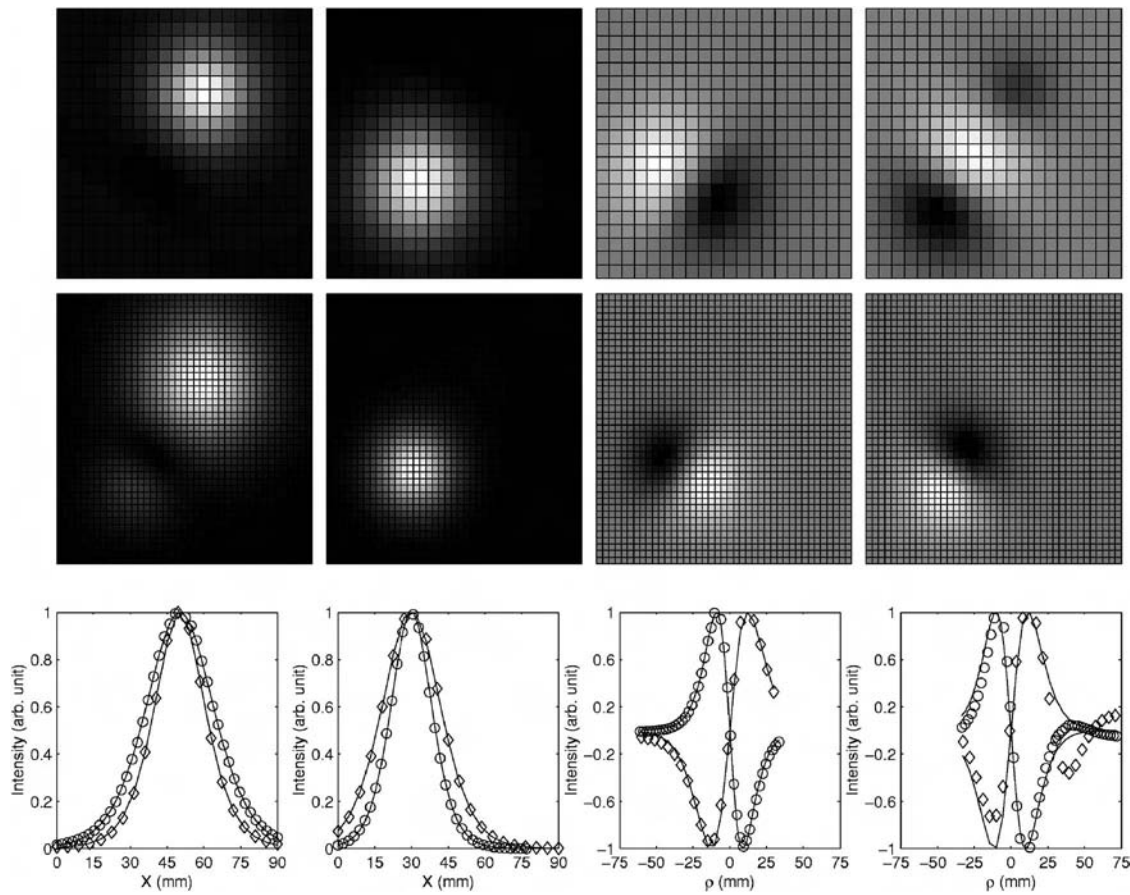
Fig. 3 Normalized independent spatial intensity distribution on the source plane, i.e., virtual sources (the first row) and on the detector plane, i.e., mixing vectors (the second row), and the least-squares fitting (the third row). The first column is for the first absorptive inhomogeneity at $(50,60,20)$ mm and the second through fourth columns are for the second scattering inhomogeneity at $(30,30,30)$ mm and represent the centrosymmetric and two dumbbell-shaped pairs of virtual sources and mixing vectors, respectively. The dumbbell comprises one bright part and its antisymmetric dark counterpart. In the third row, the profile of intensity distributions on the source plane (diamonds) and on the detector plane (circles) are displayed, and solid lines show the respective Green's function fit used for obtaining locations and strengths of objects. The X coordinate is the horizontal coordinate. The ρ coordinate is the coordinate on the symmetrical line passing through the dumbbell axis. The small dark circular region appearing near the right-upper corner of the normalized independent spatial intensity distribution on the first row and in the fourth column is an artifact.

least-squares procedure of Eq. (7). The first object is found at $(50.0,60.0,20.0)$ mm and the second one at $(30.0,30.0,30.1)$ mm. The coordinates of both objects agree to within 0.1 mm of their known locations. The strengths of the two objects are $q_1=1.00$ and $q_2=0.99$, respectively, with an error not greater than 1% of the true values.

3.2 Discrimination between Absorptive and Scattering Inhomogeneities

In the second example, one absorptive object of absorption strength of 0.01 is placed at $(50,60,20)$ mm and one scattering object of diffusion strength of negative unity (corresponding to an increase in scattering for the inhomogeneity) is placed at $(30,30,30)$ mm, respectively. We added 5% Gaussian noise to the simulated light intensity change on the detector plane.

Figure 3 shows the ICA-generated independent intensity distributions on the source and detector planes and the least-squares fitting. The first column corresponds to the absorptive inhomogeneity. The second through fourth columns corre-

spond to the scattering object, which produces one pair of centrosymmetric and two pairs of dumbbell-shaped virtual sources and mixing vectors. The absorptive inhomogeneity is found to be at $(50.2,60.3,20.2)$ mm with a strength $q_1=0.0101$. The scattering object produces three pairs (one centrosymmetric and two dumbbell-shaped) of virtual sources and mixing vectors centering around the position $(x,y)=(30,30)$ mm (see the second through fourth columns in Fig. 3). The dumbbell-shaped virtual source or mixing vector comprises one bright part and its antisymmetric dark counterpart. The resolved position and strength of the scattering object are found to be $(30.0,30.0,30.0)$ mm and $q_2=-0.99$, $(32.1,32.4,30.2)$ mm and $q_2=-0.96$, and $(31.3,30.2,27.1)$ mm and $q_2=-1.05$, respectively, through fitting to the individual pair. For the scattering object, the best result is obtained from the fitting to the first pair of centrosymmetric virtual source and mixing vector from the scattering object. Taking the position and strength of the scattering object to be that from fitting the centrosymmetric virtual source and mixing vector, the error of the resolved positions
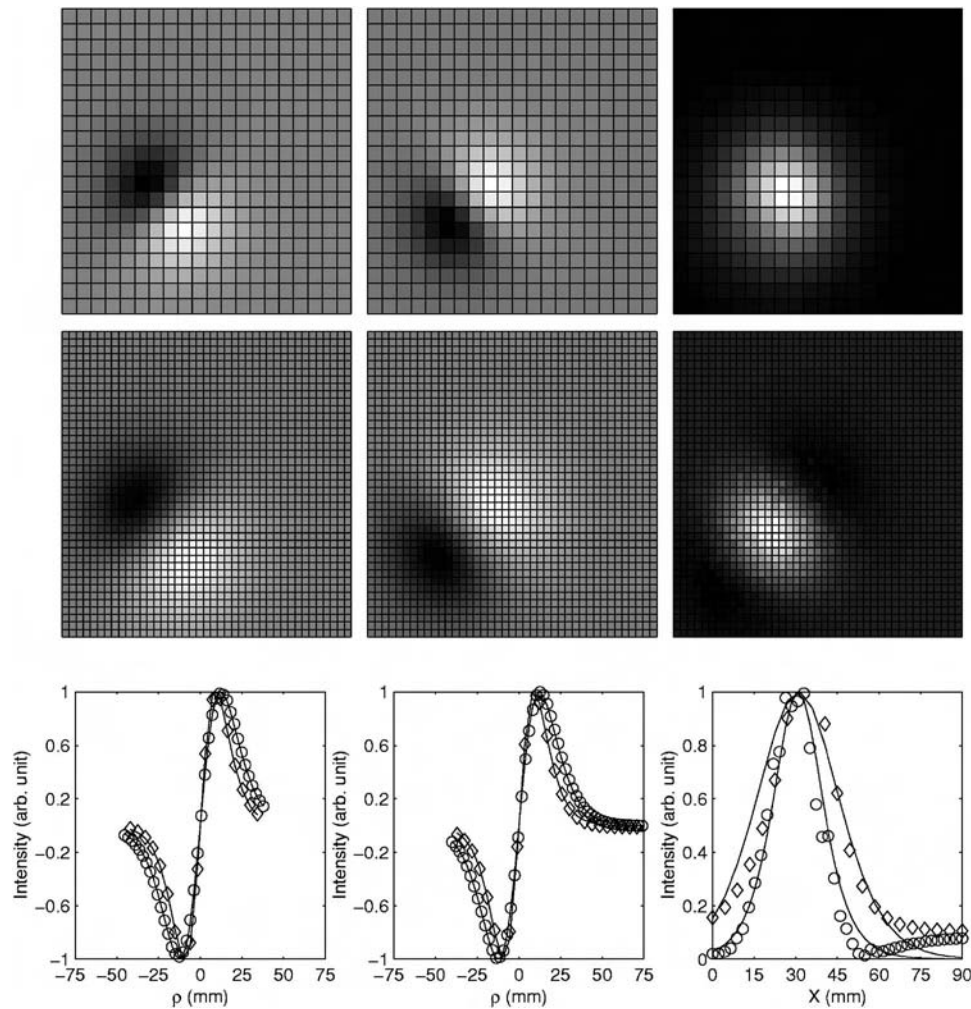
Fig. 4 Normalized independent spatial intensity distribution on the source plane (the first row) and on the detector plane (the second row), and the least-squares fitting (the third row) for one inhomogeneity located at $(30, 30, 20)$ mm with strengths of absorption $q_1=0.01$ and diffusion $q_2=1$. The first and second columns correspond to the pairs of dumbbell-shaped virtual sources and mixing vectors produced by its scattering component. The third column corresponds to its absorptive component obtained by first removing the scattering contribution. In the third row, the profile of intensity distributions on the source plane (diamonds) and on the detector plane (circles) are displayed, and solid lines show the respective Green's function fit used to obtain locations and strengths of objects. The X coordinate is the horizontal coordinate and the ρ coordinate is the coordinate on the symmetrical line passing through the dumbbell axis.

of both objects is within 0.3 mm of their known locations. The error of the resolved strengths of both objects is approximately 1% of the true values.

3.3 Colocated Absorptive and Scattering Inhomogeneities

For one complex inhomogeneity that is both absorptive and scattering, the two pairs of dumbbell-shaped virtual sources and mixing vectors produced by its scattering abnormality can be used to obtain its scattering strength. By subtracting the scattering contribution off the measured scattered wave, our procedure can be applied again to the cleaned data and we proceed to obtain its absorption strength. The third example considers a complex inhomogeneity at $(30, 30, 20)$ mm with strengths of absorption $q_1=0.01$ and diffusion $q_2=1$ (corresponding to a decrease in scattering), respectively. We added 5% Gaussian noise to the simulated light intensity change on the detector plane.

Figure 4 shows the ICA-generated independent intensity distributions on the source and detector planes and the least-squares fitting. The first and second columns correspond to the pairs of dumbbell-shaped virtual sources and mixing vectors produced by its scattering component. The position and strength of this diffusive component is obtained to be $(32.7, 33.0, 20.5)$ mm and $q_2=0.95$, and $(31.7, 30.1, 20.4)$ mm and $q_2=0.96$ by fitting the two individual dumbbell-shaped pairs, respectively. The position and strength of the diffusive component is found to be $(30.9, 30.9, 20.4)$ mm and $q_2=0.95$ if both dumbbell-shaped virtual sources and mixing vectors are used in fitting. The third column of Fig. 4 corresponds to its absorptive component obtained by first removing the scattering contribution from the measured scattered wave. The depth and strength of the absorption component is found to be $(30.8, 30.7, 32.7)$ mm and $q_1=0.0091$.
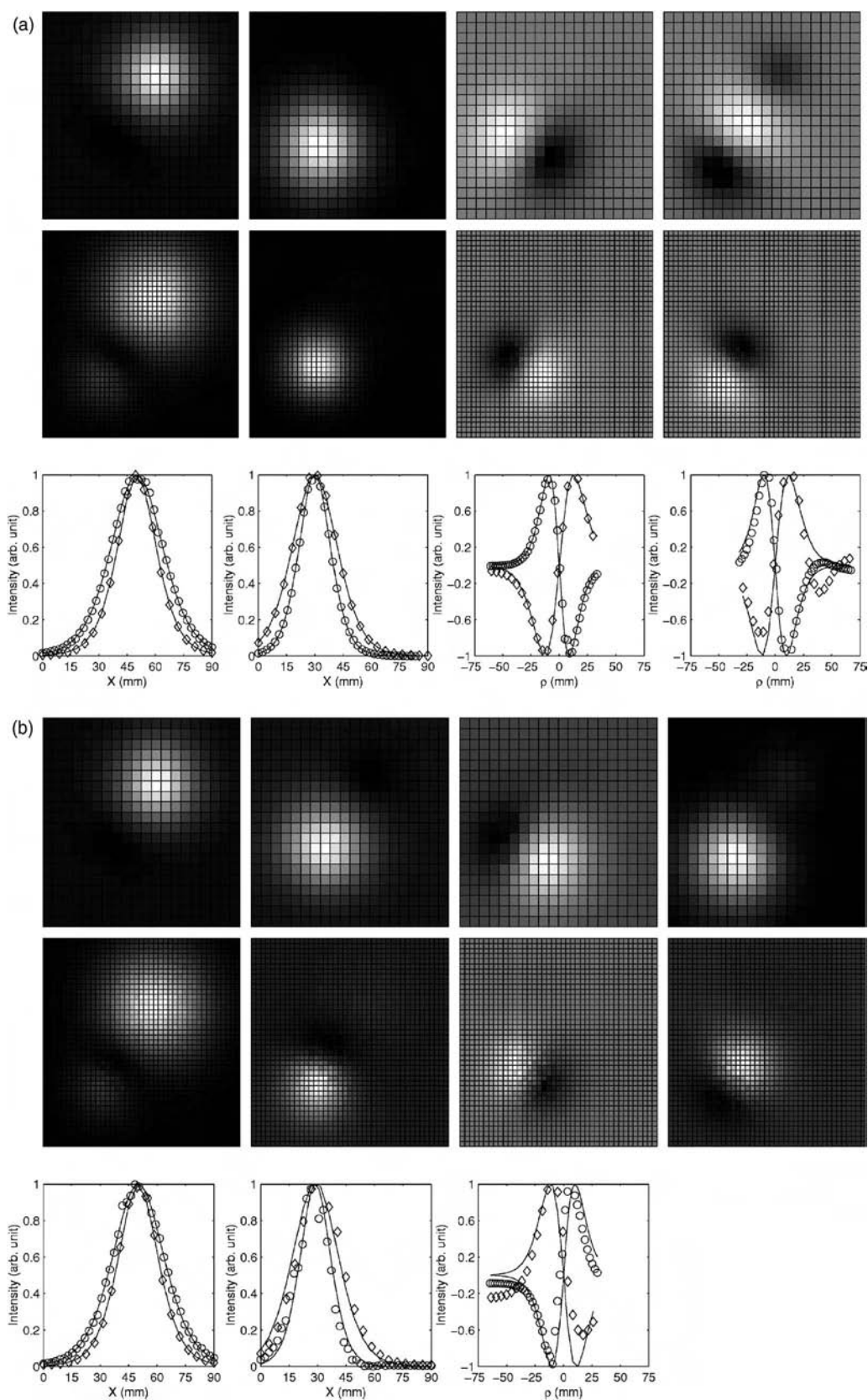
Fig. 5 Same as Fig. 3 with (a) 10% and (b) 20% Gaussian noise. The dumbbell-shaped virtual source on the source plane in the fourth column of (b) is deformed and the least-squares fitting is not shown.

Table 1 Comparison of known and OPTICA determined positions and strengths of absorption (Abs) and scattering (Sca) inhomogeneities under different levels of Gaussian noise.

Noise	Target	Known Position (x, y, z) (mm)	Known Strength	Resolved Position (x, y, z) (mm)	Resolved Strength	Error in Position (mm)	Error in Strength (%)
5%	Abs	(50, 60, 20)	0.01	(50.2, 60.3, 20.2)	0.0101	~0.3	~1
	Sca	(30, 30, 30)	−1	(30.0, 30.0, 30.0)	−0.99	~0.1	~1
10%	Abs	(50, 60, 20)	0.01	(50.2, 60.3, 20.1)	0.0101	~0.3	~1
	Sca	(30, 30, 30)	−1	(30.0, 30.1, 30.0)	−0.98	~0.1	~2
20%	Abs	(50, 60, 20)	0.01	(50.1, 60.3, 20.5)	0.0102	~0.5	~2
	Sca	(30, 30, 30)	−1	(28.9, 27.0, 32.9)	−0.59	~3	~50

The error in positioning the scattering component is less than 1 mm and the error of the resolved strength of the scattering strength is ~5%. The errors in positioning and the resolved strength of the absorptive component equal ~3 mm and ~10%, respectively, which are larger than those of the scattering component because the error is amplified when the estimated scattering component is used in subtraction off its contribution to the scattered wave in our procedure.
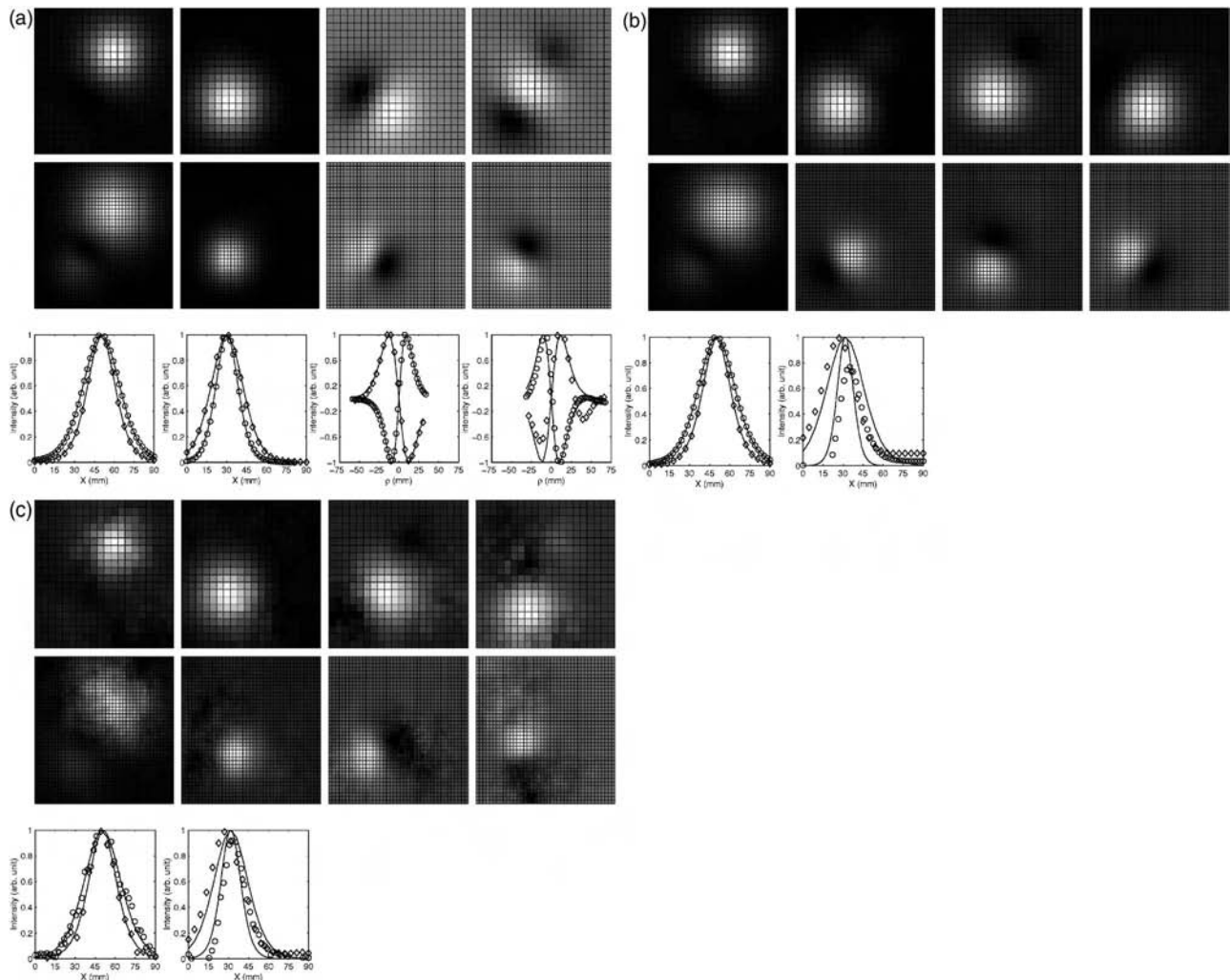

Fig. 6 Same as Fig. 3 with (a) 40, (b) 34, and (c) 10 dB background absorption uncertainty.

Table 2 Comparison of known and OPTICA determined positions and strengths of absorption (Abs) and scattering (Sca) inhomogeneities under different levels of background absorption uncertainty.

SNR (dB)	Target	Known Position (x, y, z) (mm)	Known Strength	Resolved Position (x, y, z) (mm)	Resolved Strength	Error in Position (mm)	Error in Strength (%)
40	Abs	(50, 60, 20)	0.01	(50.2, 60.3, 20.1)	0.0101	~0.3	~1
	Sca	(30, 30, 30)	−1	(30.1, 30.1, 30.0)	−0.99	~0.1	~1
34	Abs	(50, 60, 20)	0.01	(50.2, 60.3, 20.1)	0.0100	~0.3	~1
	Sca	(30, 30, 30)	−1	(31.6, 31.7, 25.3)	−0.52	~5	~50
10	Abs	(50, 60, 20)	0.01	(50.6, 60.3, 20.3)	0.0090	~0.3	~10
	Sca	(30, 30, 30)	−1	(31.7, 29.6, 31.7)	−0.78	~5	~50

3.4 Effect of Noise

To demonstrate the effect of noise on the performance of OPTICA, different levels of Gaussian noise were added to the simulated light intensity change on the detector plane.

Figure 5 shows the case presented in Fig. 3 of Sec. 3.2 with, instead, 10 and 20% Gaussian noise added to the scattered wave. The resolved absorptive inhomogeneity is at $(50.2, 60.3, 20.1)$ mm with strength 0.0101 at 10% noise, and at $(50.1, 60.3, 20.5)$ mm with strength 0.0102 at 20% noise. The resolved position and strength of the scattering object are found to be $(30.0, 30.1, 30.0)$ mm and $q_2 = -0.98$, $(32.1, 32.4, 30.4)$ mm and $q_2 = -0.95$, and $(31.4, 30.1, 27.5)$ mm and $q_2 = -1.00$, respectively, through fitting to the pair of centrosymmetric and two pairs of dumbbell-shaped virtual sources and mixing vectors [see the second to fourth columns of Fig. 5(a)], respectively, at 10% noise. The resolved values become $(28.9, 27.0, 32.9)$ mm and $q_2 = -0.59$ from fitting the pair of centrosymmetric virtual source and mixing vector [see the second column of Fig. 5(b)], and $(30.3, 32.3, 26.6)$ mm and $q_2 = -1.33$ from fitting the first pair of dumbbell-shaped virtual source and mixing vector [see the third column of Fig. 5(b)], respectively, at 20% noise. The dumbbell-shaped virtual source in the source plane, of the second pair of dumbbell-shaped virtual source and mixing vector, is deformed and the fitting is not shown [see the fourth column of Fig. 5(b)]. The deformation of dumbbell appears first in the source plane with the increase of noise as the grid spacing on the source plane is larger than that in the detector plane in the simulation.

The error in localization and characterization of scattering inhomogeneities increases rapidly with the increase of noise, from ~0.1 mm in positioning and ~2% in strength at 10% noise to ~3 mm in positioning and ~50% in strength at 20% noise. On the other hand, the effect of noise on localization and characterization of absorptive inhomogeneities is much smaller, the errors at both noise levels are less than 0.5 mm in positioning and ~2% in strength. The results in Sec. 3.2 and this section are summarized in Table 1.

3.5 Effect of Uncertainty in Background

In the examples discussed here, we have assumed the light intensities change measured on the detector plane is obtained with an exact knowledge about the background. To examine the effect of uncertainty in background optical property on the performance of OPTICA, we model the error in the estimation of the background absorption or diffusion coefficients as a uniform Gaussian random field $f(\mathbf{r})$. The Gaussian noise addressed in Sec. 3.4 is set to be zero here. OPTICA operates on a "dirty" scattering wave $-\phi_{sca}(\mathbf{r}_d, \mathbf{r}_s) + \delta\phi_{sca}(\mathbf{r}_d, \mathbf{r}_s)$, where $\delta\phi_{sca}(\mathbf{r}_d, \mathbf{r}_s)$ is the change in the scattered wave from that of a uniform background of absorption μ_a (or diffusion D) to that of a background of absorption $\mu_a + f(\mathbf{r})$ [or diffusion $D + f(\mathbf{r})$]. The magnitude of the background uncertainty is represented by the signal-to-noise ratio (SNR) defined by

$$\text{SNR(dB)} = 10 \log_{10} \frac{\sum_{\mathbf{r}_d} \sum_{\mathbf{r}_s} |\phi_{sca}(\mathbf{r}_d, \mathbf{r}_s)|^2}{\sum_{\mathbf{r}_d} \sum_{\mathbf{r}_s} |\delta\phi_{sca}(\mathbf{r}_d, \mathbf{r}_s)|^2}. \quad (13)$$

Figures 6(a)–6(c) show the case presented in Fig. 3 of Sec. 3.2 with 40, 34, and 10 dB SNR due to background absorption uncertainty, respectively. The resolved absorptive inhomogeneity is at $(50.2, 60.3, 20.1)$ mm with strength 0.0101 at 40 dB SNR, and at $(50.2, 60.3, 20.1)$ mm with strength 0.0100 at 34 dB SNR, and at $(50.6, 60.3, 20.3)$ mm with strength 0.0090 at 10 dB SNR.

The resolved position and strength of the scattering object are found to be $(30.1, 30.1, 30.0)$ mm and $q_2 = -0.99$, $(32.1, 32.9, 30.0)$ mm and $q_2 = -0.95$, and $(31.4, 30.0, 27.5)$ mm and $q_2 = -1.01$, respectively, through fitting to the pair of centrosymmetric and two pairs of dumbbell-shaped virtual sources and mixing vectors [see the second to fourth columns of Fig. 5(a)], respectively, at 40 dB SNR. The resolved values become $(31.6, 31.7, 25.3)$ mm and $q_2 = -0.52$ and $(31.7, 29.6, 31.7)$ mm and $q_2 = -0.78$ at 34 dB and 10 dB SNRs, respectively, from fitting the pair of centrosymmetric virtual source and mixing vector [see the second columns of Figs. 5(b) and 5(c)]. The dumbbell-shaped virtual sources and mixing vectors, especially the dumbbell-shaped virtual sources on the source plane are deformed and the fitting are not shown [see the third and fourth columns of Figs. 5(b) and 5(c)]. The results for the influence of background absorption uncertainty on the performance are summarized in Table 2.

Figures 7(a) and 7(b) show the case presented in Fig. 3 of Sec. 3.2 with 34 and 10 dB SNR due to background scattering
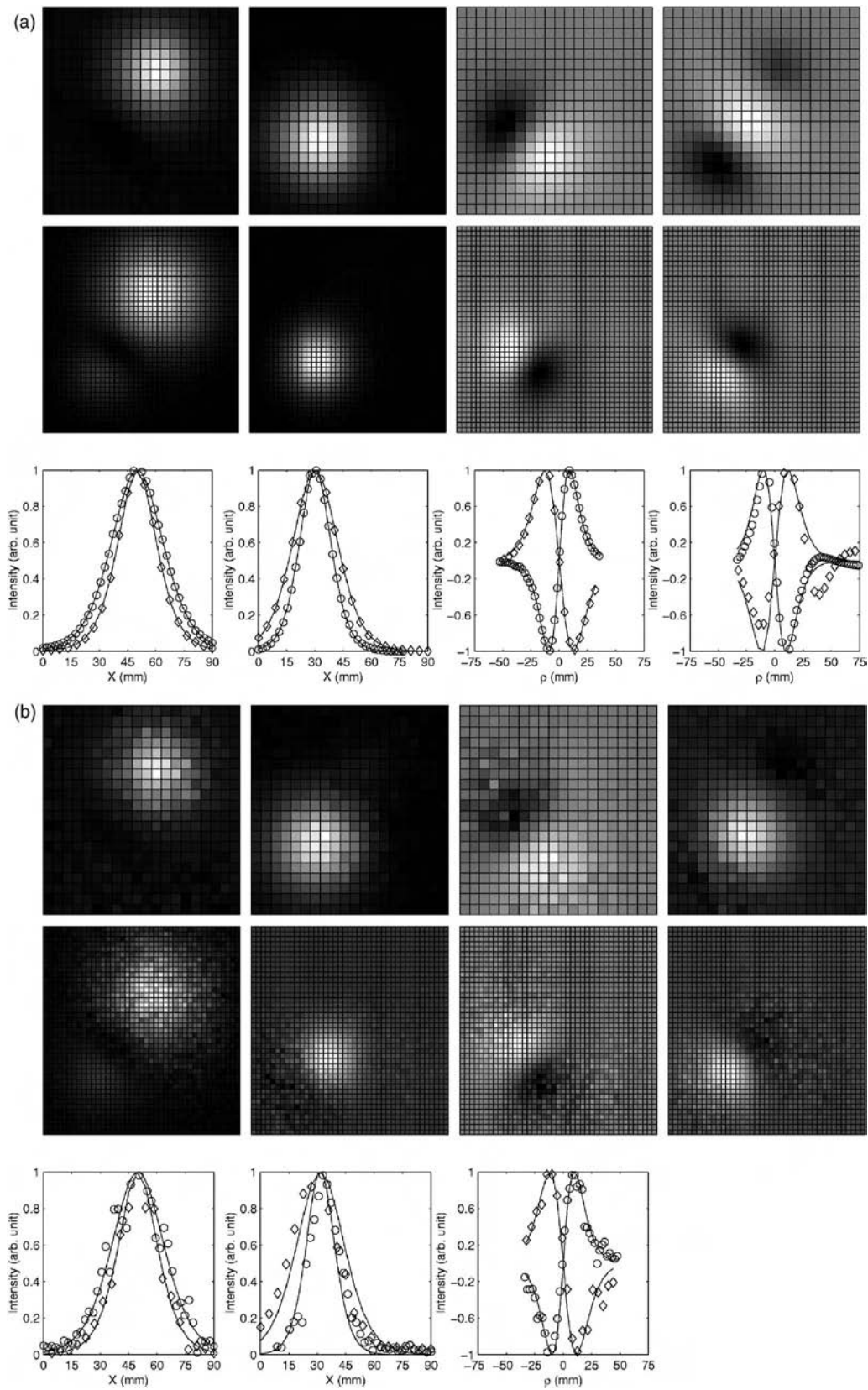
Fig. 7 Same as Fig. 3 with (a) 34 and (b) 10 dB background scattering uncertainty.

Table 3 Comparison of known and OPTICA determined positions and strengths of absorption (Abs) and scattering (Sca) inhomogeneities under different levels of background scattering uncertainty.

SNR (dB)	Target	Known Position (x, y, z) (mm)	Known Strength	Resolved Position (x, y, z) (mm)	Resolved Strength	Error in Position (mm)	Error in Strength (%)
34	Abs	(50, 60, 20)	0.01	(50.1, 60.3, 20.1)	0.0100	~0.3	~1
	Sca	(30, 30, 30)	−1	(30.0, 30.1, 30.0)	−0.99	~0.1	~1
10	Abs	(50, 60, 20)	0.01	(49.9, 60.5, 20.1)	0.0099	~0.5	~1
	Sca	(30, 30, 30)	−1	(31.7, 31.1, 32.5)	−0.75	~2.5	~25

uncertainty. The resolved absorptive inhomogeneity is at $(50.1, 60.3, 20.1)$ mm with strength 0.0100 at 34 dB SNR and at $(49.9, 60.5, 20.1)$ mm with strength 0.0099 at 10 dB SNR.

The resolved position and strength of the scattering object are found to be $(30.0, 30.1, 30.0)$ mm and $q_2 = -0.99$, $(32.2, 33.0, 30.0)$ mm and $q_2 = -0.96$, and $(32.3, 29.3, 27.1)$ mm and $q_2 = -1.08$, respectively, through fitting to the pair of centrosymmetric and two pairs of dumbbell-shaped virtual sources and mixing vectors [see the second to fourth columns of Fig. 5(a)], respectively, at 34 dB SNR. The resolved position and strength of the scattering object are found to be $(31.7, 31.1, 32.5)$ mm and $q_2 = -0.75$, $(30.9, 31.4, 27.5)$ mm and $q_2 = -1.08$, respectively, through fitting to the pair of centrosymmetric and the first pair of dumbbell-shaped virtual sources and mixing vectors [see the second to fourth columns of Fig. 5(b)] at 10 dB SNR. The results for the influence of background scattering uncertainty on the performance are summarized in Table 3.

The uncertainty in the background absorption or diffusion coefficients affects the performance of OPTICA in a similar fashion as the noise does discussed in Sec. 3.4. The error in localization and characterization of scattering inhomogeneities increases rapidly while the error in localization and characterization of absorptive inhomogeneities only increases mildly with the increase of the uncertainty in the background optical property. The uncertainty in background scattering has a less adverse effect on the performance of OPTICA than that in background absorption.

4 Discussion

The simulational study of OPTICA presented in this paper demonstrates its potential in optical imaging of objects in turbid media. It was shown to be able to locate and characterize absorptive and scattering inhomogeneities within highly scattering medium. In particular, OPTICA can discriminate between absorptive and scattering inhomogeneities and locate and characterize complex inhomogeneities, which is both absorptive and scattering. The accuracy of localization and characterization of inhomogeneities is high. In the cases investigated for concentrated inhomogeneities within a tissue-emulating slab of thickness of 50 mm, the errors in resolved object locations are not greater than 1 mm and the errors in the resolved optical strengths are ~2% under favorable noise levels and reliable background estimations.

Noise at higher levels and/or larger uncertainty in the optical property of the background medium makes it difficult to discriminate between absorptive and scattering inhomogeneities. In such a situation, other corroborative evidence, such as multiwavelength measurements, are required to determine the nature of inhomogeneities. Noise at higher levels and/or larger uncertainties in the optical property of the background medium also introduces larger errors in localization and characterization of scattering inhomogeneities. The accuracy of localization and characterization of absorptive inhomogeneities is only mildly affected by the amount of noise and/or uncertainty in the range investigated.

OPTICA unmixes inhomogeneities based on the mutual statistical independence between them and does not rely on a Gaussian distribution of light intensity on the surface of the embedding medium. OPTICA has several salient features. First, OPTICA provides the independent components due to the inhomogeneities with minimal processing of the data and does not have to resort to any specific light propagation model for obtaining this information. Specific light propagation models are needed only in the later stage to determine location and optical strength. Second, different geometries, or even an arbitrary shaped boundary, can be used with OPTICA. Although we used the slab geometry in the work reported in this paper, the approach does not depend on any specific geometry. Third, the approach is fast and is amenable to near real-time detection and localization of objects in a turbid medium, which is a key consideration for *in vivo* medical imaging.

As is well known, the diffusion approximation to RTE, which is widely used in inverse image reconstruction, does not apply when the separation between any two of the source, the inhomogeneity and the detector is small, or when there are clear regions in the medium. A special treatment is also required when the medium has aligned microstructures, such as myofibrils, axons, or collagen fibers in tissues.[43] The fact that a prior assumption of a specific model of light propagation in the medium is not assumed in the identification of independent components by ICA and is required only in a Green's function analysis of the retrieved independent component is desirable, especially in situations that demand a more complex model than the conventional DA. Performing the fitting procedure for each identified independent component is much simpler and more transparent than matching the measured light intensity to a forward model iteratively. The quality of reconstruction of OPTICA is expected to be higher than the

conventional approach when only an imperfect forward model is available.

OPTICA is most suited to detect small objects. Given its ability to identify low-contrast small objects, the approach is expected to be especially useful for detection of tumors at their early stages of development.

References

1. G. Muller, R. R. Alfano, S. R. Arridge, J. Beuthan, E. Gratton, M. Kaschke, B. R. Masters, S. Svanberg, and P. van der Zee, Eds., *Medical Optical Tomography: Functional Imaging and Monitoring*, Vol. IS11 of SPIE Institute Series, SPIE Press, Bellingham, WA (1993).
2. A. Yodh and B. Chance, "Spectroscopy and imaging with diffusing light," *Phys. Today* **48**, 38–40 (1995).
3. M. A. O'Leary, D. A. Boas, B. Chance, and A. G. Yodh, "Experimental images of heterogeneous turbid media by frequency-domain diffusing-photon tomography," *Opt. Lett.* **20**, 426–428 (1995).
4. S. K. Gayen and R. R. Alfano, "Emerging optical biomedical imaging techniques," *Opt. Photonics News* **7**, 17–22 (1996).
5. J. C. Hebden, S. R. Arridge, and D. T. Delpy, "Optical imaging in medicine: I. Experimental techniques," *Phys. Med. Biol.* **42**, 825–840 (1997).
6. S. R. Arridge and J. C. Hebden, "Optical imaging in medicine: II. Modelling and reconstruction," *Phys. Med. Biol.* **42**, 841–853 (1997), (eng).
7. W. Cai, S. K. Gayen, M. Xu, M. Zevallos, M. Alrubaiee, M. Lax, and R. R. Alfano, "Optical tomographic image reconstruction from ultrafast time-sliced transmission measurements," *Appl. Opt.* **38**, 4237–4246 (1999).
8. S. R. Arridge, "Optical tomography in medical imaging," *Inverse Probl.* **15**, R41–R93 (1999).
9. D. Grosenick, H. Wabnitz, H. H. Rinneberg, K. T. Moesta, and P. M. Schlag, "Development of a time-domain optical mammograph and first in vivo applications," *Appl. Opt.* **38**, 2927–2943 (1999).
10. V. Chernomordik, D. Hattery, A. H. Gandjbakhche, A. Pifferi, P. Taroni, A. Torricelli, G. Valentini, and R. Cubeddu, "Quantification by random walk of the optical parameters of nonlocalized abnormalities embedded within tissuelike phantoms," *Opt. Lett.* **25**, 951–953 (2000).
11. V. A. Markel and J. C. Schotland, "Inverse scattering for the diffusion equation with general boundary conditions," *Phys. Rev. E* **64**, 035601 (2001).
12. A. H. Hielscher and S. Bartel, "Use of penalty terms in gradient-based iterative reconstruction schemes for optical tomography," *J. Biomed. Opt.* **6**, 183–192 (2001).
13. M. Xu, M. Lax, and R. R. Alfano, "Time-resolved Fourier optical diffuse tomography," *J. Opt. Soc. Am. A* **18**, 1535–1542 (2001).
14. B. A. Brooksby, H. Dehghani, B. W. Pogue, and K. D. Paulsen, "Near-infrared (NIR) tomography breast image reconstruction with a priori structural information from MRI: algorithm development for reconstructing heterogeneities," *IEEE J. Sel. Top. Quantum Electron.* **9**, 199–209 (2003).
15. H. Dehghani, B. W. Pogue, S. P. Poplack, and K. D. Paulsen, "Multiwavelength three-dimensional near-infrared tomography of the breast: initial simulation, phantom, and clinical results," *Appl. Opt.* **42**, 135–145 (2003).
16. *Topics in Biomedical Optics*, J. C. Hebden, D. A. Boas, J. S. George, and A. J. Durkin, Eds., pp. 2869–3329, a special issue of *Appl. Opt.* **42** (2003).
17. W. Cai, M. Xu, and R. R. Alfano, "Three dimensional radiative transfer tomography for turbid media," *IEEE J. Sel. Top. Quantum Electron.* **9**, 189–198 (2003).
18. L. Wang, P. P. Ho, C. Liu, G. Zhang, and R. R. Alfano, "Ballistic 2-D imaging through scattering walls using an ultrafast optical Kerr gate," *Science* **253**, 769–771 (1991).
19. R. R. Alfano, X. Liang, L. Wang, and P. Ho, "Time-resolved imaging of translucent droplets in highly scattering media," *Science* **264**, 1913–1914 (1994).
20. W. Cai, M. Lax, and R. R. Alfano, "Analytical solution of the elastic Boltzmann transport equation in an infinite uniform medium using cumulant expansion," *J. Phys. Chem. B* **104**, 3996–4000 (2000).
21. W. Cai, M. Lax, and R. R. Alfano, "Analytical solution of the polarized photon transport equation in an infinite uniform medium using cumulant expansion," *Phys. Rev. E* **63**, 016606 (2000).
22. M. Xu, W. Cai, M. Lax, and R. R. Alfano, "Photon migration in turbid media using a cumulant approximation to radiative transfer," *Phys. Rev. E* **65**, 066609 (2002).
23. A. D. Klose and A. Hielscher, "Fluorescence tomography with simulated data based on the equation of radiative transfer," *Opt. Lett.* **28**, 1019–1021 (2003).
24. A. H. Gandjbakhche, G. H. Weiss, R. F. Bonner, and R. Nossal, "Photon path-length distributions for transmission through optically turbid slabs," *Phys. Rev. E* **48**, 810–818 (1993).
25. A. H. Gandjbakhche, V. Chernomordik, J. C. Hebden, and R. Nossal, "Time-dependent contrast functions for quantitative imaging in time-resolved transillumination experiments," *Appl. Opt.* **37**, 1973–1981 (1998).
26. A. N. Tikhonov and A. V. Groncharsky, Eds., *Ill-Posed Problems in the Natural Sciences*, MIR, Moscow (1987).
27. P. Comon, "Independent component analysis—a new concept?" *Signal Process.* **36**, 287–314 (1994).
28. A. J. Bell, "Information theory, independent component analysis, and applications," in *Unsupervised Adaptive Filtering*, Vol. I, S. Haykin, Ed., pp. 237–264, Wiley, New York (2000).
29. D. Nuzillard and J.-M. Nuzillard, "Application of blind source separation to 1-D and 2-D nuclear magnetic resonance spectroscopy," *IEEE Signal Process. Lett.* **5**, 209–211 (Aug. 1998).
30. R. Vigário, J. Särelä, V. Jousmäki, M. Hämäläinen, and E. Oja, "Independent component approach to the analysis of EEG and MEG recordings," *IEEE Trans. Biomed. Eng.* **47**, 589–593 (2000).
31. A. Hyvärinen, J. Karhunen, and E. Oja, *Independent Component Analysis*, Wiley, New York (2001).
32. J.-F. Cardoso, "Blind signal separation: statistical principles," *Proc. IEEE* **86**, 2009–2025 (1998).
33. A. Hyvärinen and E. Oja, "Independent component analysis: algorithms and applications," *Neural Networks* **13**, 411–430 (2000).
34. S. Chandrasekhar, *Radiative Transfer*, Dover, New York (1960).
35. M. Xu, W. Cai, M. Lax, and R. R. Alfano, "A photon transport forward model for imaging in turbid media," *Opt. Lett.* **26**, 1066–1068 (2001).
36. P. M. Morse and H. Feshbach, *Method of Theoretical Physics*, Vols. I and II, McGraw-Hill, New York (1953).
37. M. Lax, V. Nayaramamurti, and R. C. Fulton, "Classical diffusion photon transport in a slab," in *Laser Optics of Condensed Matter*, J. L. Birman, H. Z. Cummins, and A. A. Kaplyanskii, Eds., pp. 229–237, Plenum, New York (1987).
38. J. X. Zhu, D. J. Pine, and D. A. Weitz, "Internal reflection of diffusive light in random media," *Phys. Rev. A* **44**, 3948–3959 (1991).
39. R. C. Haskell, L. O. Svaasand, T.-T. Tsay, T.-C. Feng, M. S. McAdams, and B. J. Tromber, "Boundary conditions for the diffusion equation in radiative transfer," *J. Opt. Soc. Am. A* **11**, 2727–2741 (1994).
40. S. R. Arridge, "Photon-measurement density functions. Part I: Analytic forms," *Appl. Opt.* **34**, 7395–7409 (1995).
41. S. R. Arridge and M. Schweiger, "Photon-measurement density functions. Part 2: Finite-element-method calculations," *Appl. Opt.* **34**, 8026–8037 (1995).
42. H. Heusmann, J. Kölzer, and G. Mitic, "Characterization of female breasts *in vivo* by time resolved and spectroscopic measurements in near infrared spectroscopy," *J. Biomed. Opt.* **1**, 425–434 (1996).
43. J. Heino, S. Arridge, J. Sikora, and E. Somersalo, "Anisotropic effects in highly scattering media," *Phys. Rev. E* **68**, 031908 (2003).

Three-dimensional optical tomographic imaging of scattering objects in tissue-simulating turbid media using independent component analysis

M. Alrubaiee, M. Xu, S. K. Gayen, M. Brito, and R. R. Alfano[a]
Institute for Ultrafast Spectroscopy and Lasers, Physics Department, The City College of New York and the Graduate School of the City University of New York, 138th Street at Convent Avenue, New York, New York 10031

An information-theory-based approach for the detection and three-dimensional localization of scattering targets embedded in a turbid medium, such as a tumor in the breast, is introduced. The approach uses multisource illumination of the medium, multidetector transillumination signal acquisition, and independent component analysis of the information theory for target detection and localization. The efficacy of the approach is demonstrated by detecting and obtaining location information about scattering targets embedded in human breast tissue-simulating turbid media of thickness 50 times the transport mean-free path. © *2005 American Institute of Physics*.
[DOI: 10.1063/1.2130547]

Detection and localization of scattering targets within a turbid medium is a challenging problem with diverse practical applications, such as imaging of a breast tumor, identification of mines in coastal water, and detection of an airplane, or, structures through cloud and fog cover. A recent study involving 35 319 patients underscores the influence of primary tumor location on breast cancer prognosis, and makes it imperative that breast cancer detection modalities obtain three dimensional (3D) location of the tumor relative to the axilla.[1] Optical detection of targets in a turbid medium makes use of the difference in optical properties, such as scattering coefficient, absorption coefficient, index of refraction, and fluorescence between the targets of interest and the intervening medium.[2] Multiple scattering of light by the turbid medium produces a noise background that deteriorates the contrast, blurs the image, and in severe cases makes direct transillumination imaging impossible. Inverse image reconstruction approaches that are commonly used to retrieve image information have to deal with the fact that inverse problems are ill posed, and attain different measures of success with ~1 cm spatial resolution.[3]

This article introduces an alternative approach for detection and 3D localization of targets (optical inhomogeneities) embedded inside a highly scattering turbid medium. The approach makes use of transmitted light signal collected by multiple detectors following multiple-source illumination of the turbid medium containing the targets. The resulting multiple angular views provide robust data that is analyzed using the independent component analysis (ICA) (Ref. 4) of information theory to determine the locations of targets relative to the medium boundaries with millimeter accuracy. We refer to this optical domain application of ICA as OPTICA to distinguish it from other applications. While OPTICA may be used for the detection and localization of absorptive, scattering, and fluorescent targets, this letter focuses on scattering targets.

The perturbation in the light intensity distribution on the boundaries of the medium, the scattered wave field, due to scattering inhomogeneities is given by[5]

$$\phi_{\mathrm{sca}}(\mathbf{r}_d,\mathbf{r}_s) = -\int d^3r\,\delta D(\mathbf{r})c\nabla_r G(\mathbf{r}_d,\mathbf{r})\cdot\nabla_r G(\mathbf{r},\mathbf{r}_s),\quad (1)$$

in the diffusion approximation (DA). Here, $\mathbf{r}_s$, $\mathbf{r}$, and $\mathbf{r}_d$ are the positions of the source, the inhomogeneity and the detector, respectively, $\delta D = D_{\mathrm{obj}} - D$ is the difference between the diffusion coefficient of the object, D_{obj} and that of the medium, D, c is the speed of light in medium, and $G(\mathbf{r},\mathbf{r}_s)$ and $G(\mathbf{r},\mathbf{r}_d)$ are source-target and target-detector Green's functions, respectively. While the formalism, detailed elsewhere and tested for simulated data,[6] is applicable for different sample sizes and shapes, Green's functions for the slab geometry[7] are used here since rectangular slab samples were used in experiments.

Under the assumption that the scattering inhomogeneities are localized in a few regions within the turbid medium, Eq. (1) may be rewritten as

$$-\phi_{\mathrm{sca}}(\mathbf{r}_d,\mathbf{r}_s) = \sum_{j=1}^{n} g_z(\mathbf{r}_j,\mathbf{r}_d)q_j g_z(\mathbf{r}_j,\mathbf{r}_s)$$
$$+ \sum_{j=1}^{n} \rho_{dj}\cos\theta_d g_\perp(\mathbf{r}_j,\mathbf{r}_d)q_j\rho_{sj}\cos\theta_s g_\perp(\mathbf{r}_j,\mathbf{r}_s)$$
$$+ \sum_{j=1}^{n} \rho_{dj}\sin\theta_d g_\perp(\mathbf{r}_j,\mathbf{r}_d)q_j\rho_{sj}\sin\theta_s g_\perp(\mathbf{r}_j,\mathbf{r}_s),$$
$$(2)$$

where $q_j = \delta D(\mathbf{r}_j)cV_j$ is the strength of the jth scattering inhomogeneity of volume, V_j located at $\mathbf{r}_j$, $\rho_{dj} = [(x_d - x_j)^2 + (y_d - y_j)^2]^{1/2}$, $\rho_{sj} = [(x_s - x_j)^2 + (y_s - y_j)^2]^{1/2}$, and θ_d and θ_s are the polar angles of $\mathbf{r}_d - \mathbf{r}_j$, and $\mathbf{r}_s - \mathbf{r}_j$, respectively, g_z, and $g_\perp$ are the longitudinal and transverse components of the Green's functions, and the summation is over all the inhomogeneities. The contribution to ϕ_{sca} from the jth inhomogeneity consists of three terms. These three terms may be interpreted as contributions from three "virtual sources" $q_j g_z(\mathbf{r}_j,\mathbf{r}_s)$, $q_j\rho_{sj}\cos\theta_s g_\perp(\mathbf{r}_j,\mathbf{r}_s)$, and $q_j\rho_{sj}\sin\theta_s g_\perp(\mathbf{r}_j,\mathbf{r}_s)$ weighted by $g_z(\mathbf{r}_j,\mathbf{r}_d)$, $\rho_{dj}\cos\theta_d g_\perp(\mathbf{r}_j,\mathbf{r}_d)$, and $\rho_{dj}\sin\theta_d g_\perp(\mathbf{r}_j,\mathbf{r}_d)$, respectively. The first virtual source, $q_j g_z(\mathbf{r}_j,\mathbf{r}_s)$ is centrosymmetric, the other two are dumbbell
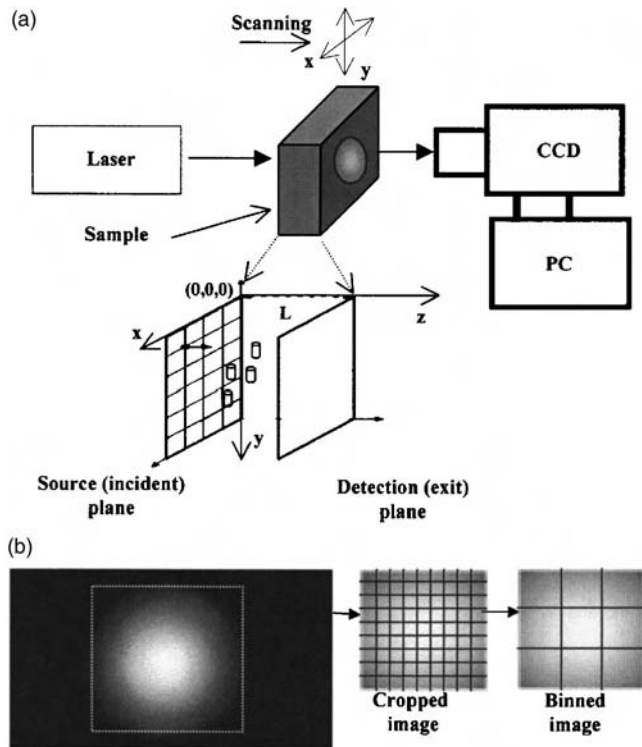
[a]Electronic mail: alfano@scisun.sci.ccny.cuny.edu

FIG. 1. (a) A schematic diagram of the experimental arrangement. Inset shows a 2D array of horizontal and vertical points in the input plane that are scanned across the laser beam. (b) A typical raw image recorded by the CCD, and how it is cropped and binned for analysis.

shaped and orthogonal to each other. The centrosymmetric virtual source makes the dominant contribution to ϕ_{sca}, compared to the other two. The detected fraction of ϕ_{sca} on the exit plane (also referred to as the detection plane) of the sample is a weighted linear mixture of contributions from $3n$ virtual sources, if there are n scattering targets within the medium. All virtual sources are assumed to be statistically independent.

Independent component analysis of the measured ϕ_{sca} can then retrieve the "virtual sources" and corresponding weighting matrices.[6] The contribution of each target to ϕ_{sca} on the detection plane (and also on the source plane) can be obtained as a two-dimensional (2D) independent intensity distribution (IID). IID due to a target may be looked upon as the light intensity pattern that a source located at the target position would generate on the detection (or source) plane. The 3D location of the target relative to sample boundaries is estimated from fits of these OPTICA generated IID to the model Green's functions.

The experimental arrangement for demonstrating the efficacy of OPTICA is shown schematically in Fig. 1. Continuous-wave 784 nm radiation from a diode laser delivered by a 200-μm-optical fiber was used for illuminating the

entrance face (henceforth referred to as the "source plane") of the slab sample. Multiple source illumination was realized in practice by step scanning the slab sample along the horizontal (x) and vertical (y) directions across the laser beam. A camera lens collected the diffusely transmitted light on the opposite face of the slab (henceforth referred to as the "detection plane") sample and projected it onto the sensing element of a cooled charged couple device (CCD) camera. Each illuminated pixel of the 1024×1024 pixels of the CCD camera could be regarded as a detector. For illumination of every scanned point on the source plane, the CCD camera recorded the diffusely transmitted intensity pattern on the detection plane.

Two different samples were used in the experiments reported here. The first sample was a 250 mm$\times$250 mm $\times$50 mm transparent plastic cell filled with Intralipid-10% suspension in water. The concentration of Intralipid-10% was adjusted to provide a transport length ℓ_t of $\sim$2 mm at 784 nm. A $\sim$9-mm-diameter glass sphere filled with a suspension of 0.707 μm diameter polystyrene spheres in water was the scattering target. The microspheres do not absorb 784 nm light, and their concentration was adjusted to provide a scattering length, ℓ_s of $\sim$0.0188 mm, transport length ℓ_t of $\sim$0.133 mm, and anisotropy factor, $g \sim 0.858$. The location of the center of the target was (25 mm, 25 mm, 21 mm) with respect to the front upper left corner of the sample cell [see inset of Fig. 1(a)]. This sample was used to test the predictions of the theoretical formalism.

The second sample was a 166-mm-long, 82-mm-wide, and 55-mm thick scattering slab cast from a suspension of titanium dioxide particles and a near-infrared dye in epoxy resin containing four cylindrical scattering targets.[8] The slab material had an optical transport length of $\sim$1.1 mm, and absorption coefficient of 0.006 mm^{-1}. Each of the four cylinders had a length of 5 mm, a diameter of 5 mm, absorption coefficient equal to that of the slab material, and scattering coefficients 4, 2, 1.5, and 1.1 times higher than that of the slab. The center of each cylinder was located in the plane halfway between the front and back surfaces of the slab, and their known coordinates are presented in Column 3 of Table I. The second sample was used to test the efficacy of OPTICA on a breast-simulating specimen. Sample 1 was scanned in an x-y array of 21×21 grid points with a step size of 2.5 mm across the laser beam, while Sample 2 was scanned in a 20×18 array of same step size.

Figure 1(b) presents a typical 2D raw image of the detection plane recorded by the CCD camera for illumination of a grid point in the source plane. Similar 2D raw images are recorded for every scanned grid point on the source plane. As Fig. 1(b) further shows, each raw image is then cropped to select out the information-rich region, and binned to enhance the signal-to-noise ratio. All the binned images are then added and an average image (henceforth, referred to as

TABLE I. Comparison of the known and OPTICA determined positions of the targets in Sample 2.

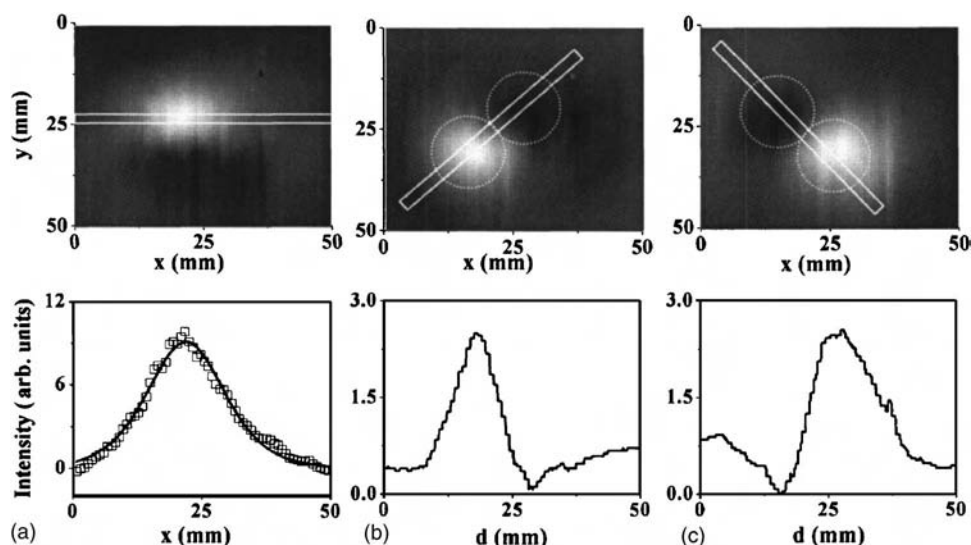| Target No.	$\mu_{s,\mathrm{target}}/\mu_{s,\mathrm{slab}}$	Known position (x,y,z) mm	Observed position (x,y,z) mm	Error $(\Delta x, \Delta y, \Delta z)$
1	4	(60, 60, 27.5)	(62, 63, 28.1)	(2, 3, 0.6)
2	2	(47, 30, 27.5)	(48, 33, 28.9)	(1, 3, 1.4)
3	1.5	(33, 60, 27.5)	(33, 62, 27.1)	(0, 2, 0.4)
4	1.1	(20, 30, 27.5)	(18, 33, 32.6)	(2, 3, 5.1)

FIG. 2. Independent 2D spatial intensity distributions at the detection plane of the scattering sphere in Sample 1 generated by OPTICA: (a) The centrosymmetric component. (b) and (c) the dumbbell shaped components. The white dotted circles in the images presented in (b) and (c) are provided as guide for the eyes to show the high intensity and low intensity areas of the dumbbell. The white rectangles in the images are the regions that are integrated over to generate the spatial profiles. In the lower frame of (a), the solid line represents a Green's function fit to the experimental data represented by open squares.

as the "reference image") is generated to serve as the background. The difference between the reference image and the mth binned image is proportional to the perturbation in light intensity distribution on the detection plane, $\phi_{sca,m}$ for illumination of the mth grid point. All the $\phi_{sca,m}$'s are then stacked, and used as input for independent component analysis.

OPTICA generated 2D independent intensity distributions (IIDs) at the detection plane for the single scattering target in Sample 1 are presented in the upper frames of Figs. 2(a)–2(c). The corresponding spatial intensity profiles integrated over the areas enclosed by white dashed boxes appear in the lower frames. As predicted by the theoretical formalism, three intensity distributions from three virtual sources corresponding to the single scattering target are observed. The spatial intensity profile of Fig. 2(a) is symmetric about the vertical centerline (centrosymmetric), the profile of Fig. 2(b) has a peak followed by a dip, and that of Fig. 2(c) has a dip followed by a peak, and resemble the predicted dumbbell shape. The location of the target determined from the Green's function fit of the intensity distribution is (23 mm, 25 mm, 22 mm) which agrees well with the known position of (25 mm, 25 mm, 21 mm). The relative peak intensity of the centrosymmetric component is approximately four times larger than that of the dumbbells. For more highly scattering samples and with a decrease in the signal-to-noise ratio, the dumbbell-shaped components get much reduced in intensity, and may not be observable. It should be mentioned that an absorptive target generates only a centrosymmetric IID.

The results of OPTICA measurements on Sample 2 are summarized in Table I, that compares the known locations of all 4 targets with those obtained from this approach. Except for Target No. 4, coordinates of other targets are obtained within 0–3 mm (a standard deviation of ~2 mm) of the respective known positions. The larger error in the estimated location of Target No. 4 may be due to its low contrast and

hence higher susceptibility to noise. Overall, the errors in location estimates are smaller than the target dimensions even for a breast-simulating scattering medium.

What is remarkable about the OPTICA approach is that even at this initial stage of development it could detect and locate all four scattering targets, including the weakest target with a scattering coefficient just 1.1 times the background and hence was considered to be "rather unlikely to be found."[8] For highly scattering medium (such as Sample No. 2), only the centrosymmetric virtual sources corresponding to scattering targets could be observed. Additional information, such as measurements at different wavelengths are needed for identification of the target as a scatterer or an absorber. Although the DA was used in this case, OPTICA does not depend on any specific light propagation model, and can be used with other models. This feature makes OPTICA a more general approach applicable for a variety of scattering media where DA may not hold. OPTICA is suited for detection of small inhomogeneities on mm scale, and has the potential for detection and localization of tumors in the breast at early stages of growth.

[1] N. Kroman, J. Wohlfahrt, H. T. Mouridsen, and M. Melbye, Int. J. Cancer **105**, 542 (2003).
[2] S. K. Gayen and R. R. Alfano, Opt. Photonics News **7**, 22 (1996).
[3] S. R. Arridge, Inverse Probl. **15**, R41 (1999).
[4] P. Comon, Signal Process. **36**, 287 (1994).
[5] M. Xu, M. Lax, and R. R. Alfano, J. Opt. Soc. Am. A **18**, 1535 (2001).
[6] M. Xu, M. Alrubaiee, S. K. Gayen, and R. R. Alfano, J. Biomed. Opt. **10**, 051705 (2005).
[7] M. Lax, V. Narayanamurti, and R. C. Fulton, in *Laser Optics of Condensed Matter*, edited by J. L. Birman, H. Z. Cummins, and A. A. Kaplyanskii (Plenum, New York, 1987), pp. 229–237.
[8] D. J. Hall, J. C. Hebden, and D. T. Delpy, Appl. Opt. **36**, 7270 (1997).

Three-dimensional optical tomography of objects in turbid media using the 'round-trip matrix'

W. Cai, M. Alrubaiee, S. K. Gayen, M. Xu, R. R. Alfano

Institute for Ultrafast Spectroscopy and lasers, Physics Department
The City College of New York, New York, NY 10031

ABSTRACT

A new algorithm based on multi-static data and vector subspace classification to eigenvectors of a round-trip matrix is introduced for optical imaging and localization of objects embedded in a turbid medium. The transport of light from multiple sources through excitation of the embedded objects to the array of detectors is represented by a response matrix that can be constructed from experimental data. The 'round-trip (RT) matrix' is constructed by multiplying the response matrix by its transpose for continuous-wave (adjoint matrix for frequency domain) illumination. Mathematically, the RT matrix is equivalent to transfer of light from the sources via the embedded objects to the array of detectors and back, and is similar to the time-reversal matrix used in the general area of array processing for acoustic and radar time-reversal imaging. The eigenvectors with leading non-zero eigenvalues of the RT matrix correspond to embedded objects, which are orthogonal to the vectors in the noise subspace. The vector subspace method along with Green's functions calculated from an appropriate model for light propagation through turbid media is then used to determine the locations of the embedded objects. We tested this algorithm in simulation for light transmitting through a 50 l_{tr} thick ($l_{tr} \sim 1$ mm is transport mean free path) parallel slab turbid medium with up to six embedded absorptive objects. The method was able to globally locate all six objects with surprising accuracy. This "round-trip tomographic imaging" approach is fast, applicable to different geometries and to different forward models.

Key words: Image reconstruction; Turbid media; Optical medical imaging; Time reversal imaging.

I. Introduction

Search of reliable and fast running approaches for inverse image reconstruction of turbid medium is an important task for optical imaging of human's tissue, breast, prostate, et al. Recent inverse algorithms, such as Newton-Raphson-Marquart algorithms [1] and that direct linear inversion of 3-D matrices [2], are time consuming. The iterative methods may not ensure that the obtained result arrives at a "global minimum," and does not converge to a "local minimum," which is not a true image.

In this paper, a new algorithm based on multi-static data and vector subspace classification to eigenvectors of a round-trip matrix is introduced for optical imaging and localization of objects embedded in a turbid medium. The transport of light, from multiple sources through excitation of the embedded objects to the array of detectors, is represented by a response matrix that can be constructed from experimental data. The 'round-trip (RT) matrix' is constructed by multiplying the response matrix by its transpose for continuous-wave (adjoint matrix for frequency domain) illumination. Mathematically, the RT matrix is equivalent to transfer of light from the sources via the embedded objects to the array of detectors and back, and is similar to the time-reversal matrix used in the general area of array processing for acoustic and radar time-reversal imaging. The time reversal imaging approaches [3-7] were successfully applied in areas of acoustic propagation and coherent propagation of electro-magnetic wave in vacuum space.

The eigenvectors with leading non-zero eigenvalues of the RT matrix correspond to embedded objects, which are orthogonal to the vectors in the noise subspace. The vector subspace method, which is called "Multiple-Signal-Classification" (MUSIC), along with Green's functions calculated from an appropriate forward mode, is then used to determine the locations of the embedded objects. We test and apply the this imaging method for light propagation in highly scattering turbid media, where the phase coherence of light no longer exist, and photons are scattered and diffuse into a broad area of detectors. The testing results using simulated data show that this method is able to globally locate the hidden objects with surprising accuracy even in a highly scattering turbid medium. When the locations of heterogeneities are found, inversion of optical parameters for these objects can be much easier than that were unknown. Since this imaging method is simple, running very fast, and can be generally applied for different geometries and other conditions, it is expected that the imaging approach have broad applications in medical imaging

II. The steps of performing imaging using the round-trip matrix

The following steps will be performed to locate the hidden objects in a turbid medium.

(1)   When a set of experimental data of light intensity injected from source R_j and received by detector R_l (l, $j = 1$, 2,...., N) is obtained, a $N \times N$ response matrix K (K_{lj} or K_{jl}) is constructed by subtracting the corresponding data in a background medium.

(2)   A $N \times N$ round-trip matrix $T = K^t K$ for the frequency domain, or $T = K^T K$ for CW case, is constructed (either SDxDS for K_{lj}; or DSxSD for K_{jl}), where K^t and K^T are, separately, the adjoint matrix and the transpose matrix of K; The T matrix is Hermitian (or real and symmetry in CW case), which had N real eigenvalues, and their eigenvectors are orthogonal with each other. All the eigenvalues and the eigenvectors of the T matrix are computed (for example, using the standard UV decomposition codes).

(3)   Separating the non-zero eigenvalues of T from the near-zero eigenvalues, the number of non-zero eigenvalues, M, determines the number of hidden objects. The corresponding eigenvectors are μ_m, $m = 1,...., M$ (each has N components). Up to this step, no physical forward model of light propagation is introduced yet.

(4)   A multiple signal classification (MUSIC) approach is used to determine the locations of M hidden objects: The 3D medium is divided to p voxels. The Green's function is calculated using a proper forward model. [$G^s(X_p, R_j)$ for SDxDS case, or $G^d(R_l, X_p)$ for DSxSD case], where X_p is the position of pth voxel. These Green's functions for the pth voxel form a vector g_p of N components. A pseudo spectrum can be computed according to the following formula:

$$P(\mathbf{X}_p) = \frac{<\mathbf{g}_p , \mathbf{g}_p>}{\left| <\mathbf{g}_p , \mathbf{g}_p> - \sum_{m=1}^{M} \left| <\mu_m , \mathbf{g}_p> \right|^2 \right|} \quad , \tag{1}$$

where the inner product $\langle A, B \rangle = \sum_{n=1}^{N} A^*(n)B(n)$. A maximum value of $P(\mathbf{X}_p)$ at $\mathbf{X}_p$, which is the position of one of the M hidden objects. By sorting of $P(\mathbf{X}_p)$, the positions of embedded objects are determined.

III. Testing based on simulation data

A slab turbid medium, with a transport mean free path $l_{tr} = 1$ mm, absorption length $l_a = 300$ mm, and thickness $z_d = 50$ mm, is divided into 20 layers. A CW light source, injected perpendicular to the $z_s = 0$ plane, scans by a 16x16 array on the x-y plane, with each pixel 5x5mm^2. An array of detectors with the same spacing is located at $z = z_d$ plane (transmission geometry). The medium is divided into 16x16x20 voxels, each of dimension 5x5x2.5 mm^3. The indices (i, j, l) represent the (x, y, z) coordinates of the voxel. Six ($M = 6$) absorbing objects are located in the medium, separately, at A(6,8,4), B(13,10,10), C(10,7,6), D(6,9,6), E(7,9,6), and F(8,12,14), with absorption difference of $\Delta\mu_a = 0.01$ mm^{-1} from the background. The objects D, and E are attached, and their x-y positions are close to that of A, hence, the objects D, E, A, are difficult to be distinguished. The objects C, D, E, are located in the same z layer.

Using a diffusion model of light propagation in slab geometry, intensities from the source array to the detector array through medium with and without hidden objects are calculated and subtracted. The data with adding (a) noise = 0, (b) noise = 5% are produced as simulated "experimental" data. The dimension of the K matrix (sources are in row, and detectors are in column) is $N = 16 \times 16 = 256$. Then, the matrix $T = K^T K$ (DSxSD) is constructed from simulated data, and 256 eigenvalues of T and corresponding eigenvectors is computed.

The computed data of eigenvalues are sorted in descent order and are listed in the *first column* of the table 1. At this stage (without calculation of the Green's function), we have seen that there are 6 largest eigenvalues, which can be clearly distinguished from other near-zero eigenvalues. Hence, the signal space is determined as $M = 6$ from simulated data. Next step, the diffusion model is used to calculate the Green's functions from a voxel to the detectors (need not that from the sources to the voxel), and the pseudo-spectrum (16x16x20) is calculated according to Eq. (1) using these Green's function and the computed M eigenvectors in the signal space. The values of pseudo-spectrum are sorted in descent order. The largest values of them and the corresponding positions of voxels are listed in the *second column* in the table 1.

We see that for the zero-noise case, the six non-zero eigenvalues are more 10 orders of magnitude larger than other near-zero eigenvalues. All six largest pseudo-values are located at the correct locations we set previously, and their values are more 10 orders of magnitude larger than the value at their neighborhood locations. This result is magically well.

For the case of 5% noise, the values of the near-zero eigenvalues greatly increase, but still one order of magnitude less than smallest non-zero eigenvalue, as shown on the ***third column*** in the table 1. The pseudo-values, shown in the ***fourth column*** of the table 1, at locations (13,10,10), (10,7,6), and (8,12,14), although have greatly reduced comparing to the zero-noise case, are clearly maximum comparing to their neighborhood, that is the well resolved case we discuss before. The pseudo-value at (6,8,4) is also a maximum. The pseudo-values at (6,9,6) and (7,9,6) can be regarded as a local maximum, although the maximum for object at (7,9,6) has been little bit moved. All these peaks are among the largest values in 256x20 values in the pseudo-spectrum. This image result is quite well comparing to that of other image reconstruction approaches.

(a) simulated data (no noise)

eigen value	i	j	l	P(i,j,l)
5.878267e-10	13	10	10	3.071404e+15
4.244296e-11	7	9	6	2.982245e+15
1.584357e-11	10	7	6	1.275038e+15
3.861900e-12	6	9	6	7.403212e+14
1.094898e-13	8	12	14	5.251203e+14
8.792975e-15	6	8	4	4.044517e+14
3.239483e-25	6	8	3	5912.727
7.226278e-26	7	9	5	4089.3306
6.936422e-26	6	8	5	3767.8683
6.689055e-26	7	9	7	3053.547
6.411725e-26	6	9	5	2816.3402
6.326671e-26	10	7	5	2485.2019
6.055272e-26	6	9	7	2065.8781

. . . .

(b) simulated data (5% noise)

eigen value	i	j	l	P(i,j,l)
5.878410e-10	13	10	10	51384.399
4.239479e-11	10	7	6	23437.917
1.582402e-11	8	12	14	18144.901
3.858276e-12	10	7	5	2200.9195
1.136558e-13	6	8	4	2105.3805
-1.473045e-14	10	7	7	1697.181
-9.815438e-15	6	8	3	1476.2329
-8.444224e-15	7	9	5	1327.5666
7.192133e-15	6	8	5	1271.6959
-6.470322e-15	7	9	4	977.96331
6.156419e-15	7	9	6	924.28242
-4.679483e-15	6	8	2	923.62776
-4.508637e-15	13	10	9	791.29503
4.028535e-15	10	7	4	711.70233
3.657569e-15	6	9	6	656.91035
3.372298e-15	7	9	3	625.15459
3.087945e-15	6	9	7	596.06539
-2.838656e-15	13	10	11	554.31961

. . .   .

IV.   Advantages of the approach

(1) This approach is simple and running very fast. If the weight matrix in the above example is written, it is 256x256 in row and 256x20 in column. In "round-trip matrix" imaging, the problem is reduced to make a singular value decomposition of a matrix of 256 in row and 256 in column. Computation can be completed in a few minute on a personal computer.

(2) As shown above, the positions of objects can be globally determined, and the image results are quite well.

(3) Only one kind Green's function is needed, either that from sources to a voxel or that from a voxel to detectors. Hence, the requirement for the forward model is reduced. Especially, error due to use of the diffusion model in computation of the Green's function from the sources to voxels can be avoided, if only the Green's function from voxels to detectors is required.

(4) This approach can be generally used under many different conditions, either parallel geometry or cylindrical geometry.

(5) The background medium may be uniform or non-uniform, as long as the Greens function of the background can be estimated. For example, this algorithm may be used for imaging based on the difference of data obtained using different wavelengths.

V. Brief description of theory for the imaging using the round-trip matrix

The theoretical foundation of the above approach is based on the work by A. J. Devaney [3].

Experimental data are collected by a array of multiple-sources and multiple-detectors, which are expressed by a response matrix K. In a linear form using the Born perturbation method, the K matrix can be theoretically expressed as:

$$K = \{K_{l,j}\} = \sum_{m=1}^{M} G^d(\mathbf{R}_l, \mathbf{X}_m)\tau_m G^s(\mathbf{X}_m, \mathbf{R}_j) \equiv \sum_{m=1}^{M} g_m^d \tau_m g_m^s \tag{2}$$

or

$$K = \{K_{j,l}\} = \sum_{m=1}^{M} G^s(\mathbf{X}_m, \mathbf{R}_j)\tau_m G^d(\mathbf{R}_l, \mathbf{X}_m) = \sum_{m=1}^{M} g_m^s \tau_m g_m^d$$

where $l, j = 1, 2, \ldots, N$ are, separately, indices of detectors and sources, $m = 1, 2, \ldots, M$ is the index of hidden objects, with $M < N$; $\mathbf{R}_j$, $\mathbf{R}_l$, and $\mathbf{X}_m$ are, respectively, the positions of a source, a detector, and an object; τ_m is difference of the optical parameters (absorption and scattering) of the object from that of the background medium (the background medium may be uniform or non-uniform), and $G^s(\mathbf{X}_m, \mathbf{R}_j)$ and $G^d(\mathbf{R}_l, \mathbf{X}_m)$ are the Green's functions in the background medium. The vector $g_m = [G(\mathbf{X}_m, \mathbf{R}_1), G(\mathbf{X}_m, \mathbf{R}_2), \cdots, G(\mathbf{X}_m, \mathbf{R}_N)]$ in Eq. (1) has N components.

When data of the K matrix is obtained by measurements, a $N \times N$ round-trip matrix $T = K^\dagger K$ for the frequency domain, or $T = K^T K$ for CW case, is constructed (SDxSD for K_{lj}; or DSxSD for K_{jl}), where $K^\dagger$ and K^T are, separately, the adjoint matrix and the transpose matrix of K. This T matrix was called the "time-reversal" matrix, as time-reversal process in time-domain becomes phase conjugation in the frequency-domain through a Fourier transform. In the time-reversal experiments, a special "phase conjugate" mirror is applied, that the process after reflected from the mirror is equivalent to a time-reversal process, instead of a process along future of time. However, we do not see this time-reversal process, especially, in CW case. What we see is a round-trip from sources to detectors, and then back to sources (or, theoretically, from detectors to source, and back to detectors). Therefore, a "round-trip" matrix may be proper for description of the T matrix here. The T matrix is Hermitian (or real and symmetry in CW case), hence, its eigenvalues are real and the corresponding eigenvectors consist a complete set of orthonormal vectors.

In the many cases, it can be proved that **the rank of T matrix equals to the number of hidden objects M**, which means this matrix has M non-zero eigenvalues. The corresponding eigenvectors construct a signal subspace. The $N - M$ eigenvectors with zero eigenvalues (or near zero, in the case of presence of noise) construct a noise subspace. These two subspaces are orthogonal with each other. Use of orthogonality of eigenvectors of the T matrix is the main tool for accurately locating hidden objects in a turbid medium using time-reversal imaging.

The T matrix (for DSxSD) can be written as:

$$T = \left[\sum_{m=1}^{M} g_m^d \tau_m g_m^s\right]^* \left[\sum_{m'=1}^{M} g_{m'}^s \tau_{m'} g_{m'}^d\right] = \sum_{m=1}^{M} \sum_{m'=1}^{M} \Lambda_{m,m'} g_m^{d*} g_{m'}^d \tag{3}$$

where

$$\Lambda_{m,m'} = \tau_m \tau_{m'} < g_m^s, g_{m'}^s > = \tau_m \tau_{m'} \sum_{j=1}^{N} G^{s*}(\mathbf{X}_m, \mathbf{R}_j) G^s(\mathbf{X}_{m'}, \mathbf{R}_j) \ , \tag{4}$$

where the inner product is defined as $\left\langle A, B \right\rangle = \sum_{n=1}^{N} A^*(n) B(n)$.

For a well-resolved case, we have $< g_m^s, g_{m'}^s > \approx 0, < g_m^d, g_{m'}^d > \approx 0$ when $m \neq m'$. We interpret the quantity

$$H^d(\mathbf{r}, \mathbf{X}_m) = \sum_{n=1}^{N} G^d(\mathbf{R}_n, \mathbf{r})^* G^d(\mathbf{R}_n, \mathbf{X}_m) \ , \tag{5}$$

as being the point spread function (PSF) of the detector array, which represents an "image" of object m from measurements on N detectors in terms of the *backprojection* of the outgoing wave Green's function. If the object m' is located far enough from the object m, that is $H(\mathbf{X}_{m'}, \mathbf{X}_m) \approx 0$, then these two objects are regarded to be well resolved.

If all M objects are well resolved each other, we have $\Lambda^s_{mm'} = \Lambda^s_m \delta_{mm'}$ and $T = \sum\limits_{m=1}^{M} \Lambda^s_m g^{d*}_m g^d_m$,

$\Lambda^s_m = |\tau_m|^2 \rho^s_m$, with a normalized factor $\rho^s_m = <g^s_m, g^s_m>$. In this case, we can prove that M non-zero eigenvectors

are precisely $\mu_m = g^{d*}_m /(\rho^d_m)^{1/2}$, and the corresponding non-zero eigensvalues are $|\tau_m|^2 \rho^s_m \rho^d_m$.

[prove] $\quad T g^{d*}_{m_0} = \sum\limits_{m=1}^{M} \Lambda^s_m g^{d*}_m g^d_m g^{d*}_{m_0} = \sum\limits_{m=1}^{M} \Lambda^s_m g^{d*}_{m_0} \rho^d_m \delta_{m,m_0} = |\tau_{m_0}|^2 \rho^s_{m_0} \rho^d_{m_0} g^{d*}_{m_0}$. $\qquad$ (6)

The non-zero eigenvalue of mth object is related to the optical strength of the object, and the Green's function from this object to the sources and detectors. In the well resolved case, when the eigenvectors $\mu_m(j)$ in the signal subspace are computed using a Green's function based a forward model. The locations of targets can be determined by:

$$\psi_m(\mathbf{r}) = \sum\limits_{j=1}^{N} G(\mathbf{r}, \mathbf{R}_j)\mu_m(j) = \frac{1}{(\rho_m)^{1/2}} H^*(\mathbf{r}, \mathbf{X}_m) \;, \qquad (7)$$

where $H(\mathbf{r}, \mathbf{X}_m)$ is the point spread function of a target located at $\mathbf{X}_m$. The maximum of $H(\mathbf{r}, \mathbf{X}_m)$ at $\mathbf{r}$ determines the position of mth target.

The M eigenvectors span the signal subspace P_S. Because T is a NxN matrix, other N–M eigenvectors have zero eigenvalues and span the noise subspace P_N, and $P_S + P_N = I$. In the case of non-well-resolved targets, the vector characterizing an object can be a linear combination of several eigenvectors in the signal subspace, hence, Eq. (7) is not available for determining locations of objects. A MUSIC approach is applied to determine the locations of targets, which uses the property that any linear combination of eigenvectors in the signal subspace must be orthogonal to the vectors in the noise subspace. We use a forward model to calculate the Green's function at test location $\mathbf{X}_p$:

$$g(\mathbf{X}_p) = [G(\mathbf{X}_p, \mathbf{R}_1), G(\mathbf{X}_p, \mathbf{R}_2), \cdot \cdot \cdot, G(\mathbf{X}_p, \mathbf{R}_N)] \quad . \qquad (8)$$

MUSIC uses a pseudo-spectrum to determine the target locations. After the eigenvectors in the noise space u_j are obtained, the following pseudo-spectrum can be computed:

$$P(\mathbf{X}_p) = \frac{1}{\sum\limits_{\Lambda_j \approx 0} |\langle u_j, g(\mathbf{X}_p) \rangle|^2} \quad , \qquad (9)$$

that $P(\mathbf{X}_p)$ become large at object locations and will be small otherwise. It is more convenient to use $P_N = I - P_S$, and apply the eigenvectors in the signal space instead of the eigenvectors in the noise space. We have

$$\sum\limits_{j=M+1}^{N} \left| \left\langle \mu_j, g_p \right\rangle \right|^2 = |[I - P_S]g_p|^2 = \left| g_p - \sum\limits_{m=1}^{M} \mu_m \left\langle \mu_m, g_p \right\rangle \right|^2 = |g_p|^2 - \sum\limits_{m=1}^{M} |< \mu_m, g_p >|^2. \qquad (10)$$

The denominator of the Eq. (1) is obtained from Eq. (10). We use $\left| g_p \right|^2$ in the numerator of Eq. (1) to make the expression normalized.

VI. Summary

In this paper we test the image algorithm using the round-trip matrix to locate hidden objects in highly scattering turbid media using light signals of an array of multiple sources-detectors. The testing results using simulated data show that this method is able to globally locate the hidden objects with high accuracy in a highly scattering turbid medium. Since this image method is simple, running very fast, and can be generally applied for different geometries and other conditions, it is expected that the approach has broad applications in medical imaging.

References:
1. B. A. Brooksby, H. Dehghani, B. W. Pogue, K. D. Paulsen, "Near-Infrared (NIR) Tomography Breast Image Reconstruction with A Priori Structural Information From MRI: Algorithm Development for Reconstructing Heterogeneities", IEEE IJSQEN **9** p199-209 (2003).
2. Y. Tao, Y. Wang, Y. Pei, W. Zhu, R. L. Barbour, "Frequency-domain optical imaging of absorption and scattering distribution using a born iterative method," J. Opt. Soc. Am. A **14** 325-342 (1997).
3. A. J. Devaney, "Super-resolution Processing of Multi-static Data Using Time Reversal and MUSIC", Preprint.
4. A. J. Devaney, "Time Reversal Imaging of Obscured Targets From Multstatic Data", Preprint.
5. C. Prada, J. L. Thomas, M. Fink, "The iterative time reversal process: Analysis of the convergence", J. Acoustical Society of America, **97**, 62 (1995).
6. C. Prada, S. Manneville, D. Spokiansky, and M. Fink, " Decomposition of the time reversal operator: Detection and selective focusing on two scatterers", J. Acoustical Society of America, **99**, 2067 (1996).
7. P. Stoica, R. Moses, *Introduction to Spectral Analysis*, Prentice Hall, New jersey (1997).

Fluorescence optical tomography using independent component analysis to detect small targets in turbid media

M. Alrubaiee, M. Xu, S. K. Gayen, and R. R. Alfano
Institute for Ultrafast Spectroscopy and Lasers, Physics Department
The City College of New York, 138th Street at Convent Avenue, New York, NY 10031

ABSTRACT

A new approach for optical fluorescence tomographic imaging of targets in a turbid medium that uses the independent component analysis (ICA) from information theory is presented. Fluorescence signals from targets embedded in a turbid medium are measured on the boundary of the medium using a multi-source excitation and a multi-detector acquisition scheme. Differences between excitation and fluorescence wavelengths enable sensitive, minimal-background signal acquisition. ICA of the fluorescence signal on the medium boundary sorts out the embedded objects, and their locations are obtained from Green's function analysis based on any appropriate light propagation model. Fluorescence tomographic imaging experiments were carried out using Intralipid-10% suspension in water contained in a 50-mm thick rectangular transparent plastic cell as the turbid medium, and small glass spheres containing indocyanine green (ICG) solution as fluorescent targets. The near-infrared (NIR) fluorescence was excited using 785 nm light, and monitored over a narrow band around 830 nm. The transport mean free paths at 785 nm and 830 nm were 1.01 mm and 1.14 mm, respectively. The approach could image and determine the position of an ICG filled sphere of radius as small as 4 mm. It is applicable to small objects, different medium geometries, and amenable to near real time imaging applications.

Keyword: Near-infrared fluorescence imaging, imaging through turbid media, tissue-like phantom, inverse image reconstruction, independent component analysis.

1. INTRODUCTION

The advent of novel fluorescence beacons and contrast agents with ability to attach themselves to a desired large cluster of abnormal cells or organelles,[1] and fluoresce when excited with light of appropriate wavelength make fluorescence tomography attractive for detection and diagnosis of tumors in human body organs, such as, breast and prostate. Direct imaging approaches fail to provide accurate location of fluorescent targets embedded in a turbid medium[2,3] Researchers then resort to tomographic image reconstruction (TIR) schemes that use fluorescence signals measured from the surface of the specimen, an appropriate model for light propagation, and numerical algorithms to reconstruct fluorescent target(s) inside the specimen.[4-9]

We introduce a novel optical tomography approach that uses independent components analysis[10,11] of information theory to analyze the fluorescence signal excited by a multi-source illumination scheme and measured by a multi-detector signal acquisition arrangement providing a variety of spatial and angular views essential for three-dimensional (3D) localization and characterization of the target. We refer to this approach as fluorescence OPTICA.

2. THEORY

Fluorescence tomography requires accounting for propagation of excitation light beams that induce fluorescence from embedded targets, and that of the fluorescence emitted by the localized targets to the detectors. In fluorescence OPTICA, the incident light at wavelength λ_x propagates from the source point r_s at the input (or, source) plane to the target located at position r inside the medium. Fluorescence at wavelength λ_m propagates from target at r to the detector at r_d. The propagation of excitation and fluorescent light beams is described by coupled diffusion equations at the excitation and emission wavelengths [8,9]

The fluorescence signal $U_m(r_d, r_s, \omega)$ can be expressed in terms of the two Green's functions $G_x(r, r_s, \omega)$ and $G_m(r_d, r, \omega)$ describing light propagation from the source at r_s to the target at r at the excitation wavelength λ_x and the light propagation from the target to the detector at r_d at the emission wavelength λ_m. The subscripts x and m refer to the

quantities associated with the excitation and emission wavelengths, respectively. Assuming the jth fluorescent target is contained in volume V_j centered at r_j, the fluorescence signal under illumination by a unit point source at r_s is given by

$$U_m(\mathbf{r}_d,\mathbf{r}_s,\omega) = \sum_{j=1}^{J} G_m(\mathbf{r}_d,\mathbf{r}_j,\omega) f_j(\omega) G_x(\mathbf{r}_j,\mathbf{r}_s,\omega) \qquad (1)$$

where $f_j(\omega) = \gamma(\mathbf{r}_j) c V_j/[1-i\omega\tau(r_j)]$ represents the fluorescence strength of the jth inhomogeneity, γ is the fluorescent yield, and τ is the fluorescence lifetime. The contribution of jth source, $f_j G_x(r_j, r_s, \omega)$ is weighted by a mixing vector $G_m(\mathbf{r}_d,\mathbf{r}_j,\omega)$ and all the weighted sources are mixed to produce the detected signal $U_m(\mathbf{r}_d,\mathbf{r}_s,\omega)$. ICA assumes that the signals from the fluorescent targets are statistically independent, and that the measured signal is a weighted mixture of contributions from these independent sources.[10,11] By seeking the maximal mutual independence, both fluorescent sources and mixing vectors can be obtained by independent component analysis of the multi-source multi-detector data set $U_m(\mathbf{r}_d, \mathbf{r}_s, \omega)$.

3. EXPERIMENTAL ARRANGEMENT

Figure 1 shows schematically the experimental setup used for testing the fluorescence OPTICA approach. The turbid used in the experiment was Intralipid-10% suspension in water contained in a 250 mm x 250 mm x 50 mm transparent plastic cell. The concentration of Intralipid-10% was adjusted to provide a transport length $l_t \sim 1mm$ at 785 nm. The fluorescent target consists of glass sphere with a hook attached to a white thin string as shown in Fig. 2(a). The sphere is filled with a solution of Indocyanine green (ICG) dye in water. The absorption coefficient of the ICG solution at 785 nm is 11.5 mm^{-1}. To test how small an object could be observed, we used three different spheres with diameters 12 mm, 9 mm and 4 mm in turn. A 785-nm continuous wave (CW) laser beam was delivered through a ~200-μm diameter optical fiber and focused to a ~1 mm spot onto the input surface of the sample cell. A computer-controlled translation stage scanned the sample in a set of 10 x 10 grid points (step size = 2.5-mm), in the x-y plane perpendicular to the incident beam realizing a multi-source illumination scheme. For illumination at everyone of these points a 1024 x 1024 pixels cooled charge couple device (CCD) camera acquired a 2-D fluorescence image of the exit surface (opposite to the input surface) of the cell. The fluorescence spectrum of ICG in water, when excited at 785-nm, spans the wavelength range of 790-966 nm as shown in the inset of Fig. 1. We used a narrow-band filter centered at 830-nm to acquire a fraction of the fluorescence, and discriminate against the much more intense laser excitation beam. The images were stored in a personal computer for subsequent analysis by the numerical algorithm of fluorescence OPTICA.
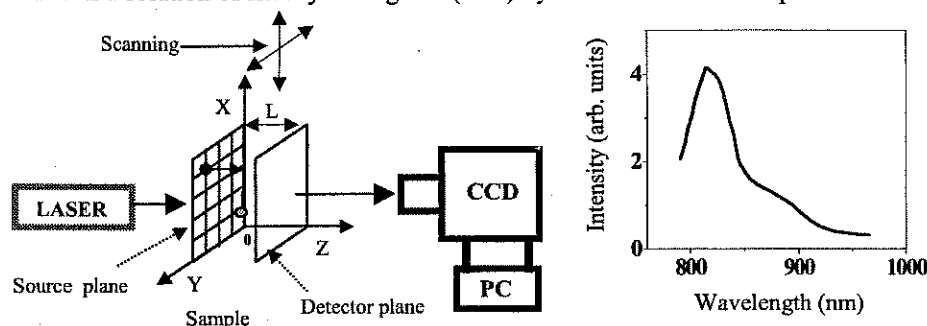
Fig.1 A schematic diagram of the experimental arrangement for fluorescence OPTICA. The inset shows the fluorescence spectrum of ICG solution in water

4. RESULTS

A typical 2-D fluorescence image of the exit surface of the turbid medium recorded by the CCD camera is shown in Figure 2(b). The fluorescent target in this case was the 4-mm diameter sphere. Independent components analysis used the set of 100 images to generate independent intensity distribution on source and detector planes, as shown in Figures 2(c) and 2(d), respectively. The Green's function (solid line) fit to these intensity distributions represented by squares for the source plane and by circles for the detector plane are shown in Figures 3(a) and 3(b), respectively. The x-y-z co-ordinates of the fluorescence target were estimated to be approximately, $x = 15$ mm, $y = 15$ mm, and $z = 16$ mm, which are in excellent agreement with the known location of $x = 15$ mm, $y = 15$ mm, and $z = 15$ mm. This result is for the smallest of the spheres, and hence the most difficult of the three cases. The locations of the other two spheres were readily observed using the fluorescence OPTICA.
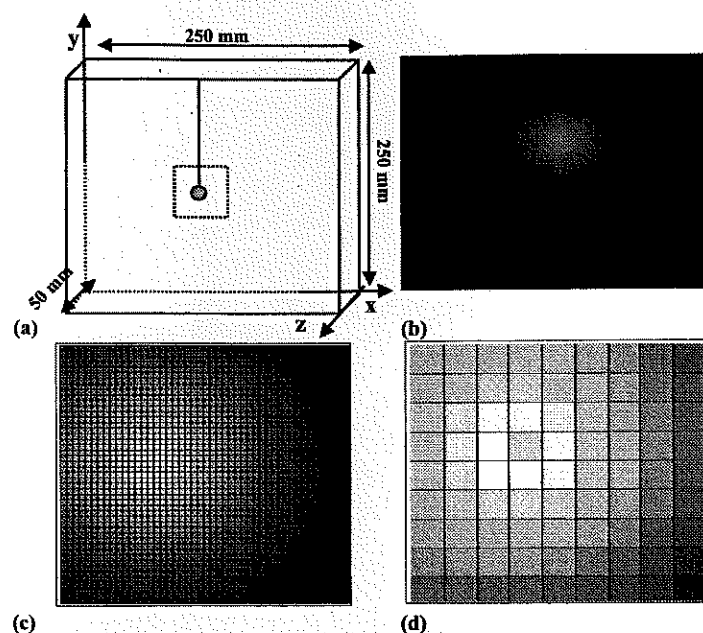
Fig. 2. (a) A schematic diagram showing the positions of fluorescence sphere filled with ICG in the Intralipid-10% suspension, (b) Fluorescence image at 830-nm. Independent spatial intensity distributions (independent components) in (c) the entrance, and (d) exit plane of the specimen.
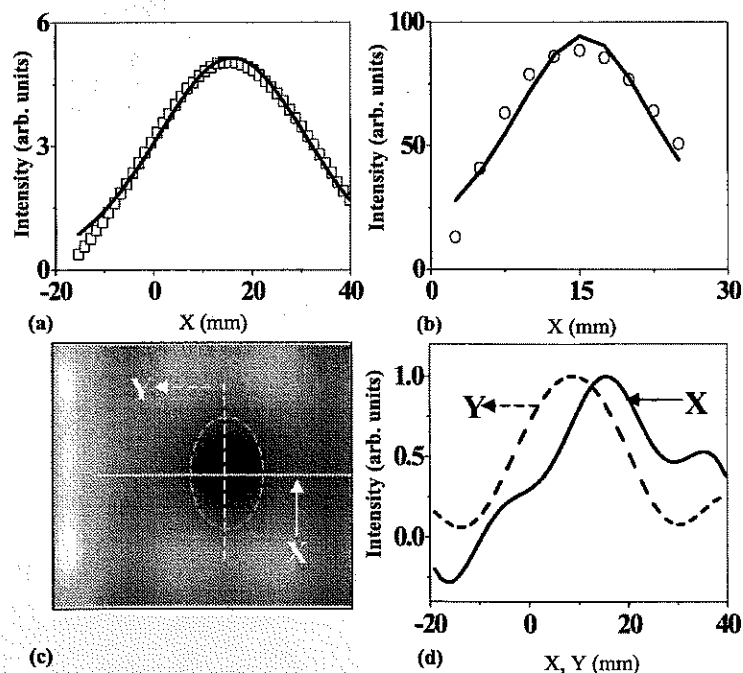
The shape of the 4-mm diameter object was reconstructed by using back-projection Fourier transforms. Figure 3(c) shows the projection onto the x-y plane, and Figure 3(d) shows the corresponding spatial intensity profiles. The full width half maximum (FWHM) of the profile in the x-direction is ~16-mm, while that in the y-direction is 18 mm. We attribute this change in shape and size to the projection of the hook being superimposed onto that of the sphere. This artifact was much reduced for the 12-mm diameter sphere where the shape of the hook could be distinguished, and the FWHM of the profiles were only 14 mm, much closer to the actual value.

5. DISCUSSION

Fig. 3 (a)-(b) Green's functions (solid line) fits to Independent spatial intensity (circle) from Fig. 2 (c)-(d) respectively. (c)-(d) Shape reconstructed using back-projection Fourier transform with corresponding spatial intensity profile

The approach presented in this article effectively used a multiple source excitation (realized through scanning of the sample in the x-y plane) and multiple detectors (each pixel on the CCD may be viewed as a detector) for data acquisition providing sufficient data for extracting useful location information about the fluorescent target. While OPTICA can be used for locating absorptive and scattering targets as well,[12] the advantage for the fluorescent target is that the background light can be minimized by use of appropriate filters, making it a 'zero-background' measurement, as opposed to the situations involving absorptive and scattering targets when changes in high light levels are measured. The 3-D localization of the object is achieved with a high accuracy, and shorter computation time compared to other commonly used methods for 3-D inverse image reconstruction. The ability to discern the ~4-mm diameter ICG sphere demonstrate the potential to detect breast tumors in early stage of growth when the treatment is most effective.

ACKNOWLEDGEMENTS

REFERENCES

1. Sanjay Tyagi, Salvatore A.E. Marras, Fred Russell Kramer, "Wavelength-shifting molecular beacons", *Nature Biotechnology* **18**, 1191 (2000).
2. Alexander D. Klose, AndreasH. Hielscher, "Fluorescence tomography with simulated data based on the equation of radiative transfer" *Opt. Lett.* **28**,1019 (2003).
3. M. A. O'Leary, D. A. Boas, X. D. Li, B. Chance, A. G. Yodh, "Fluorescence lifetime imaging in turbid media", *Opt. Lett.* **21**,158 (1996).
4. W. Cai, S. K. Gayen, M. Xu, M. Zevallos, M. Alrubaiee, M. Lax, R. R. Alfano "Optical tomographic image reconstruction from ultrafast time-sliced transmission measurements," *Appl. Opt.* **38**, 4237 (1999).
5. V. Ntziachristos, "Experimental three-dimensional fluorescence reconstruction of diffuse media by use of a normalized Born approximation", *Opt. Lett.* **26**, 893 (2001).
6. S. R. Arridge, "Optical tomography in medical imaging," *Inverse Probl.* **15**, R41 (1999).
7. A. D. Kim, "Optical Diffusion of Continuous-Wave, Pulsed, and Density Waves in Scattering Media and Comparisons with Radiative Transfer", *Appl. Opt.* **37**, 5313 (1998)
8. M. S. Patterson and B. W. Pogue, "Mathematical model for time-resolved and frequency-domain fluorescence spectroscopy in biological tissues," *Appl. Opt.* **33**, 1963 (1994).
9. A. B. Milstein, S. Oh, K. J. Webb, C. A. Bouman, Q. Zhang, D. A. Boas, and R. P. Millane, "Fluorescence optical diffusion tomography," *Appl. Opt.* **42**, 3081 (2003).
10. P. Comon, *Signal-Processing* **36**, 287-104 (1994).
11. J. -F. Cardoso, "Blind signal separation: statistical principle," Proceedings of the IEEE **9**, 2009 (1998).
12. M. Alrubaiee, M. Xu, S. K. Gayen, W. Cai, and R. R. Alfano, "Time-resolved and quasi-continuous wave three-dimensional tomographic imaging of objects in tissue-like turbid media" Proceedings of SPIE Vol. **5463**, 82-85 (2004).

Optical tomography using independent component analysis to detect absorptive, scattering, or fluorescent inhomogeneities in turbid media

M. Xu, M. Alrubaiee, S. K. Gayen and R. R. Alfano

Institute for Ultrafast Spectroscopy and Lasers,
New York State Center of Advanced Technology for Ultrafast Photonic Materials and Applications,
and Department of Physics,
The City College and Graduate Center of City University of New York, New York, NY 10031

ABSTRACT

A new imaging approach for three-dimensional localization and characterization of absorptive, scattering or fluorescent objects in a turbid medium is presented and demonstrated using simulated and experimental data. This approach uses a multi-source and multi-detector signal acquisition scheme and independent component analysis (ICA) from information theory for target localization and characterization. Independent component analysis of the perturbation in the spatial intensity distribution or the fluorescent signal measured on the medium boundary sorts out the embedded objects. The location and optical characteristics (size, shape and optical property) of the embedded objects are obtained from a Green's function analysis based on an appropriate model for light propagation in the background medium and back-projections of the retrieved independent components.

Keywords: optical imaging, independent component analysis, absorption, scattering, fluorescence

1. INTRODUCTION

Optical probing of the interior of highly scattering colloidal suspensions and biological materials has attracted much attention over the last decade. In particular, biomedical optical tomography and spectroscopy using near infrared (NIR) light has been actively pursued to provide, for example, functional information about brain activities and diagnostic information about breast tumor because NIR light can penetrate deep into tissues and is sensitive to certain physiological parameters such as hemoglobin concentration and blood flow.[1-7] Both endogenous contrasts such as increased hemoglobin absorbance, and exogenous contrasts such as fluorescence agents have been studied for the purpose of medical diagnostics and prognostic measure.

Most works[4, 8-10] in imaging of endogenous or exogenous contrasts in turbid media adopt an inverse problem formalism based on the diffusion approximation or radiative transfer of light propagation in highly scattering media. A map of the spatial distribution of the endogenous contrast inside the medium is reconstructed by matching the detected light intensity change due to the contrast to that calculated by a forward model for light propagation in that medium. A map of the spatial distribution of the exogenous contrast is reconstructed, in a similar fashion, by matching the detected fluorescence to that calculated by a forward model for the propagation of the fluorescence light excited by an incident light beam in that medium. The commonly used forward models include the radiative transfer equation (RTE),[7, 10] the diffusion approximation (DA) of RTE,[4] and random walk of photons.[11]

Further author information: (Send correspondence to M. X.)
M. X.: Email: minxu@sci.ccny.cuny.edu

In this paper, we present an alternative approach using independent component analysis (ICA) of information theory to detect absorptive, scattering, or fluorescent inhomogeneities within tissue-like turbid media. We use a multi-source multi-detector scheme of data acquisition where light intensities are measured on the boundary of the medium by a two dimensional detector array when an external point source scans on the other side of the medium. The recorded data set (after removal of background signal in imaging of absorption or scattering contrasts) provides a set of observations made in multiple channels (detectors) from virtual sources (the inhomogeneities illuminated by the incident wave) over multiple discrete sampling points (the source scanning positions). Absorptive, scattering or fluorescent inhomogeneities appear as statistically independent virtual sources. These virtual sources are recovered by independent component analysis of the data set and sorts out the inhomogeneities. The location and characterization (size, shape and optical property) of inhomogeneities are obtained from a Green's function analysis based on any appropriate model of light propagation in the background medium and back-projections of the retrieved independent components. This approach is best suited for small inhomogeneities.

We refer to this information theory-inspired approach as optical imaging using independent component analysis, abbreviated as, OPTICA. ICA has been successfully applied in various other applications such as electroencephalogram and nuclear magnetic resonance spectroscopy.[12–15] The novelty of OPTICA over other ICA applications is that OPTICA associates directly the independent components to the Green's functions responsible for light propagation in the turbid medium from the inhomogeneities to the source and the detector, and therefore the retrieved independent components can be used to locate and characterize the inhomogeneities.

2. THEORY

2.1. Absorptive and scattering inhomogeneities

Absorptive and scattering inhomogeneities within a turbid medium alter the propagation of light through the medium. The alteration of the spatial distribution of the light intensity on the boundary of the medium depends on two Green's functions (propagators) $G(\mathbf{r}, \mathbf{r}_s, \omega)$ and $G(\mathbf{r}_d, \mathbf{r}, \omega)$ describing light propagation from the source at $\mathbf{r}_s$ to the inhomogeneity at $\mathbf{r}$ and from the inhomogeneity to the detector at $\mathbf{r}_d$, respectively, where ω is the modulation frequency of light.

In a parallel geometry, the scattered wave due to the presence of J absorptive inhomogeneities and J scattering inhomogeneities can be written as[16]

$$
\begin{aligned}
-\phi_{\text{sca}}(\mathbf{r}_d, \mathbf{r}_s, \omega) \;=\; & \sum_{j=1}^{J} G(\mathbf{r}_d, \mathbf{r}_j, \omega) q_j G(\mathbf{r}_j, \mathbf{r}_s, \omega) + \sum_{j=1}^{J'} g_z(\mathbf{r}_j, \mathbf{r}_d, \omega) q'_j g_z(\mathbf{r}_j, \mathbf{r}_s, \omega) \\
& + \sum_{j=1}^{J'} \rho_{dj} \cos\theta_d g_\perp(\mathbf{r}_j, \mathbf{r}_d, \omega) q'_j \rho_{sj} \cos\theta_s g_\perp(\mathbf{r}_j, \mathbf{r}_s, \omega) \\
& + \sum_{j=1}^{J'} \rho_{dj} \sin\theta_d g_\perp(\mathbf{r}_j, \mathbf{r}_d, \omega) q'_j \rho_{sj} \sin\theta_s g_\perp(\mathbf{r}_j, \mathbf{r}_s, \omega)
\end{aligned}
\tag{1}
$$

where $q_j = \delta\mu_a(\mathbf{r}_j)cV_j$ is the absorption strength of the jth inhomogeneity of volume V_j, $q'_j = \delta D(\mathbf{r}_j)cV'_j$ is the diffusion strength of the jth scattering inhomogeneity of volume V'_j, $\delta\mu_a$ and δD are the deviation of the absorption and diffusion coefficients of the inhomogeneity from that of the background medium respectively, c is the speed of light in the background medium, $\rho_{dj} = \sqrt{(x_d - x_j)^2 + (y_d - y_j)^2}$ and $\rho_{sj} = \sqrt{(x_s - x_j)^2 + (y_s - y_j)^2}$ are the projections of $\mathbf{r}_d - \mathbf{r}_j$ and $\mathbf{r}_s - \mathbf{r}_j$ on the xy plane, respectively, and θ_d and

θ_s are the azimuthal angles of $\mathbf{r}_d - \mathbf{r}_j$ and $\mathbf{r}_s - \mathbf{r}_j$, respectively. The expressions of the Green's function G and the two auxiliary functions g_z and $g_\perp$ depend on the light propagation model in the background medium.[16]

In OPTICA, the absorptive or scattering inhomogeneities illuminated by the incident wave are assumed to be *virtual sources*, and the perturbation of the spatial distribution of the light intensity on the boundary described by Eq. (1) may be considered to be a linear mixture of signals arriving from these virtual sources. One absorptive inhomogeneity is represented by one virtual source $q_j G(\mathbf{r}_j, \mathbf{r}_s)$ with a mixing vector $G(\mathbf{r}_d, \mathbf{r}_j)$. One scattering inhomogeneity is represented by three virtual sources:

$$q'_j g_z(\mathbf{r}_j, \mathbf{r}_s), \quad q'_j \rho_{sj} \cos\theta_s g_\perp(\mathbf{r}_j, \mathbf{r}_s), \quad q'_j \rho_{sj} \sin\theta_s g_\perp(\mathbf{r}_j, \mathbf{r}_s), \tag{2}$$

with mixing vectors

$$g_z(\mathbf{r}_j, \mathbf{r}_d), \quad \rho_{dj} \cos\theta_d g_\perp(\mathbf{r}_j, \mathbf{r}_d), \quad \rho_{dj} \sin\theta_d g_\perp(\mathbf{r}_j, \mathbf{r}_d) \tag{3}$$

respectively.

Owing to the statistical independence between virtual sources, independent component analysis of the recorded data set can identify prominent independent components. Each independent component consists of one virtual source and its corresponding weighting vector. The number of leading independent components is same as the number of inhomogeneities. The details of the theoretical formalism of OPTICA for absorption or scattering inhomogeneities were presented elsewhere.[16]

2.2. Fluorescent inhomogeneities

Light propagation in a highly scattering medium with fluorescent targets excited by an external source is approximately described by coupled diffusion equations at the excitation and emission wavelengths.[8, 9] The fluorescence signal $U_m(\mathbf{r}_d, \mathbf{r}_s, \omega)$ can be expressed in terms of the two Green's functions $G_x(\mathbf{r}, \mathbf{r}_s, \omega)$ and $G_m(\mathbf{r}_d, \mathbf{r}, \omega)$ describing light propagation from the source at $\mathbf{r}_s$ to the target at $\mathbf{r}$ at the excitation wavelength λ_x and the light propagation from the target to the detector at $\mathbf{r}_d$ at the emission wavelength λ_m. The subscripts x and m refer to the quantities associated with the excitation and emission wavelengths, respectively.

Assuming the jth fluorophores is contained in volume V_j centered at $\mathbf{r}_j$, the fluorescence signal under illumination by a unit point source at $\mathbf{r}_s$ is given by

$$U_m(\mathbf{r}_d, \mathbf{r}_s, \omega) = \sum_{j=1}^{J} G_m(\mathbf{r}_d, \mathbf{r}_j, \omega) f_j(\omega) G_x(\mathbf{r}_j, \mathbf{r}_s, \omega) \tag{4}$$

where $f_j(\omega) = \gamma(\mathbf{r}_j) c V_j / [1 - i\omega\tau(\mathbf{r}_j)]$ represents the fluorescence strength of the jth inhomogeneity, γ is the fluorescent yield, and τ is the fluorescence lifetime.

Eq. (4) takes exactly the same form of the scattered wave Eq. (1) for absorptive inhomogeneities only (setting $q'_j = 0$ in Eq. (1)). The jth virtual source $f_j G_x(\mathbf{r}_j, \mathbf{r}_s, \omega)$ is weighted by a mixing vector $G_m(\mathbf{r}_d, \mathbf{r}_j, \omega)$ and all the weighted virtual sources are mixed to produce the detected signal $U_m(\mathbf{r}_d, \mathbf{r}_s, \omega)$. By seeking the maximal mutual independence, both virtual sources and mixing vectors can be obtained by independent component analysis of the multi-source multi-detector data set $U_m(\mathbf{r}_d, \mathbf{r}_s, \omega)$.

Let us denote the recovered jth virtual source by $s_j(\mathbf{r}_s) \propto G_x(\mathbf{r}_j, \mathbf{r}_s, \omega)$ and the recovered corresponding mixing vector by $a_j(\mathbf{r}_d) \propto G_m(\mathbf{r}_d, \mathbf{r}_j, \omega)$. Both localization and strength of the jth object can be computed by a least square fitting procedure:

$$\min_{\mathbf{r}_j, \alpha_j, \beta_j} \left\{ \sum_{\mathbf{r}_s} \left[\alpha_j^{-1} s_j(\mathbf{r}_s) - G_x(\mathbf{r}_j, \mathbf{r}_s) \right]^2 + \sum_{\mathbf{r}_d} \left[\beta_j^{-1} a_j(\mathbf{r}_d) - G_m(\mathbf{r}_d, \mathbf{r}_j) \right]^2 \right\}. \tag{5}$$

The fitting yields the location r_j of and the two scaling constants α_j and β_j for the jth inhomogeneity. The fluorescence strength is then given by $f_j = \alpha_j \beta_j$.

The size and shape of the inhomogeneity can be estimated after the fluorescent object has been localized. The fluorescence signal due to the jth object is $U_{m_j}(\mathbf{r}_d, \mathbf{r}_s, \omega) = a_j(\mathbf{r}_d)s_j(\mathbf{r}_s)$. One can estimate the volume V_j of the jth object by its thickness profile $\Delta z_j(\rho)$ in the z direction where ρ is the lateral coordinate on the $z = z_j$ plane with z_j the z coordinate of the center of the jth object. The fluorescence signal from the jth object is approximately given by:

$$U_{m_j}(\mathbf{r}_d, \mathbf{r}_s, \omega) \simeq f_j(\omega)\frac{1}{V_j}\int G_m(\rho_d - \rho, \omega)\Delta z_j(\rho)G_x(\rho - \rho_s, \omega)d\rho \tag{6}$$

where the integration is performed over the $z = z_j$ plane, and ρ_d and ρ_s are the lateral coordinates of the detector and the source respectively. In the Fourier space, the thickness Δz_j can be solved from Eq. (6) and is given by

$$\Delta z_j(\mathbf{q}) = \frac{V_j}{f_j(\omega)}\frac{U_{m_i}(\mathbf{q} - \mathbf{q}_s, \mathbf{q}_s, \omega)}{G_m(\mathbf{q} - \mathbf{q}_s, \omega)G_x^*(\mathbf{q}_s, \omega)}. \tag{7}$$

where $\mathbf{q}$ and $\mathbf{q}_s$ are the spatial frequency on the xy plane and $*$ denotes complex conjugate. The inverse Fourier transform of $\Delta z_j(\mathbf{q})$ yields the thickness profile of the fluorescent target in the z direction. The FWHM (full width at half maximum value) and the contour of the thickness profile provide an estimation of size and shape of the jth target, respectively. This procedure to obtain size and shape of the fluorescent inhomogeneity also applies to the absorptive and scattering inhomogeneities.

3. RESULTS

The first test of OPTICA involved imaging of two absorptive inhomogeneities using simulated data. In simulation, the absorptive objects are placed at $(50, 60, 20)$mm and $(30, 30, 30)$mm, respectively, inside a slab of volume $90 \times 90 \times 50$mm^3 shown schematically in Fig. 1(a). Each inhomogeneity has a volume of $6.75 \times 6.75 \times 4.69$mm^3 and an absorption strength of unity. The absorption and diffusion coefficients of the uniform slab is $\mu_a = 1/300$mm^{-1} and $D = 1/3$mm respectively, close to that of human breast tissue.[17] The incident CW beam scans a set of 21×21 grid points covering an area of 90×90mm^2. The spacing between two consecutive grid points is 4.5mm. The light intensity on the other side of the slab is recorded by a CCD camera on 42×42 grid points covering the same area. 10% Gaussian noise was added to the simulated light intensity change on the detector plane.

Independent component analysis of the perturbation in the spatial intensity distributions provided corresponding independent intensity distributions on the source and detector planes. ICA generated independent intensity distributions on the source and detector planes are shown in Fig. 1(b), for the two absorptive inhomogeneities. Locations of the absorptive objects are obtained from fitting these independent component intensity distributions to those of the diffusion approximation in a slab by least square. The first object is found at $(50.0, 60.0, 21.1)$mm and the second one at $(30.0, 30.0, 29.9)$mm. The xy coordinates of both objects agree exactly with their known values and the z coordinate of both objects is within 1.2mm of their known center locations. The strengths of the two objects are $q_1 = 0.88$ and $q_2 = 0.88$ respectively, with an error of $\sim 12\%$ of the true values.

The thickness map for the two absorptive objects is back-projected using a formula similar to Eq. (7) and presented in Fig. 2. For each case, the Green's function at the source and detector planes (circle) are shown with the fitting in solid lines on the first row. The longitudinal thickness map of the target and the thickness profiles along X and Y directions are also displayed on the second row. Both targets are observed to have approximately
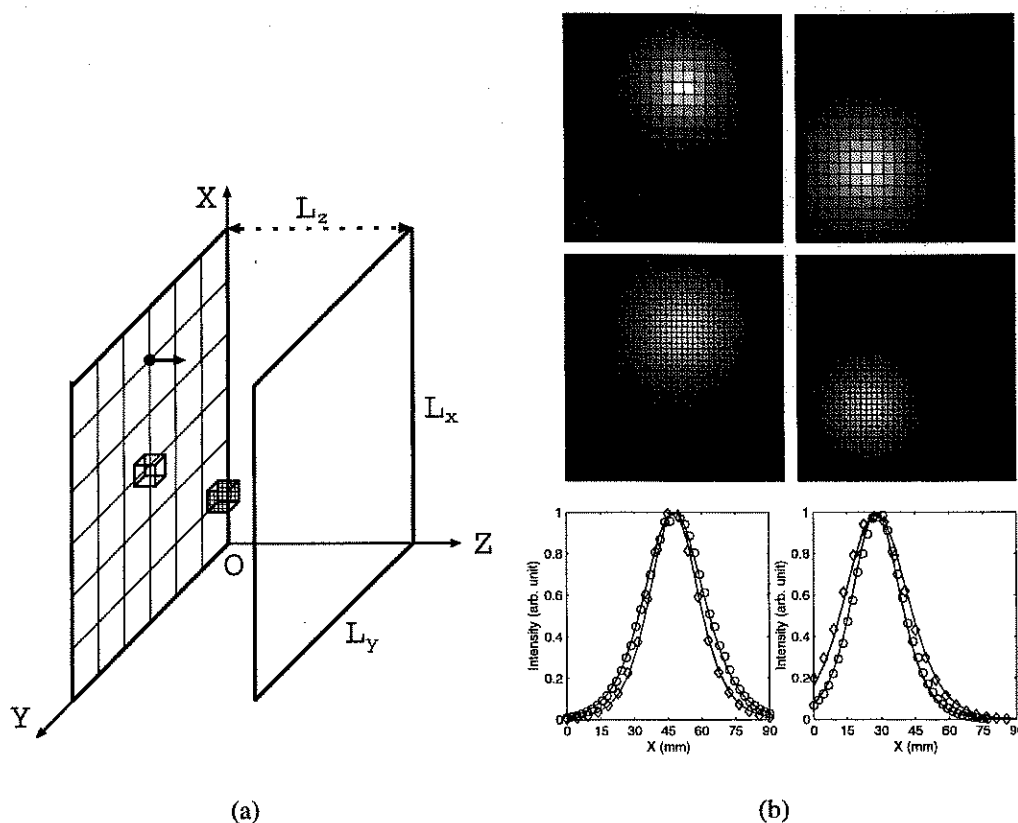
Figure 1. (a) The light intensity on one side of the slab is measured when a point source scans on the other side. Two inhomogeneities are placed at $(50, 60, 20)$mm and $(30, 30, 30)$mm inside a $90 \times 90 \times 50$mm^3 slab. (b) Normalized independent spatial intensity distributions on the source plane (the first row), the detector plane (the second row), and the least square fitting (the third row). The left column is for the first absorptive inhomogeneity at $(50, 60, 20)$mm and the right column is for the second absorptive inhomogeneity at $(30, 30, 30)$mm. On the third row, the horizontal profile of intensity distributions on the source plane (diamond) and on the detector plane (circle) are displayed, and solid lines show the respective Green's function fit used for obtaining locations and strengths of objects. The noise level is 10%.

a square shape. The FWHM of the peak for the first and the second target are found to be 16.0mm and 13.6mm, and 9.5mm and 10.5mm in the x and y directions, respectively. These values should be compared to the size of the absorptive target of 6.75mm in the xy plane. The estimation of the size and shape of the second absorptive object is more accurate as it is closer to the detector plane where the grid spacing is finer.

The second example is to image a spherical fluorescent target placed inside a 250mm×250mm × 50mm slab filled with Intralipid-10% aqueous suspension using experimental data [see Fig. 3(a)]. The fluorescent target was a 9.0mm diameter sphere filled with a solution of Indocyanine green (ICG) dye in water that could be excited in the 650nm-800nm spectral range. The wavelength of the CW incident light is $\lambda_x = 785$nm. Two long wavelength pass absorption filters were placed before the CCD camera to block the excitation wavelength and allow the fluorescence light to pass. The wavelength of the peak fluorescence light adjusted by the filtering and the camera response efficiency is about $\lambda_m = 870$nm. The Intralipid-10% suspension is diluted with pure water such that the transport mean free paths and absorption coefficients are $l_x = 1.01$mm and $\mu_{a_x} = 0.0022$mm^{-1} at the excitation wavelength and $l_{t_m} = 1.14$mm and $\mu_{a_m} = 0.0054$mm^{-1} at the emission wavelength, respectively. The sphere is placed at the position $(11, 9, 32)$mm inside the slab. The sphere is 33mm away from the input window. The point source scans over a 10×10 grid system with spacing 2.5mm between consecutive
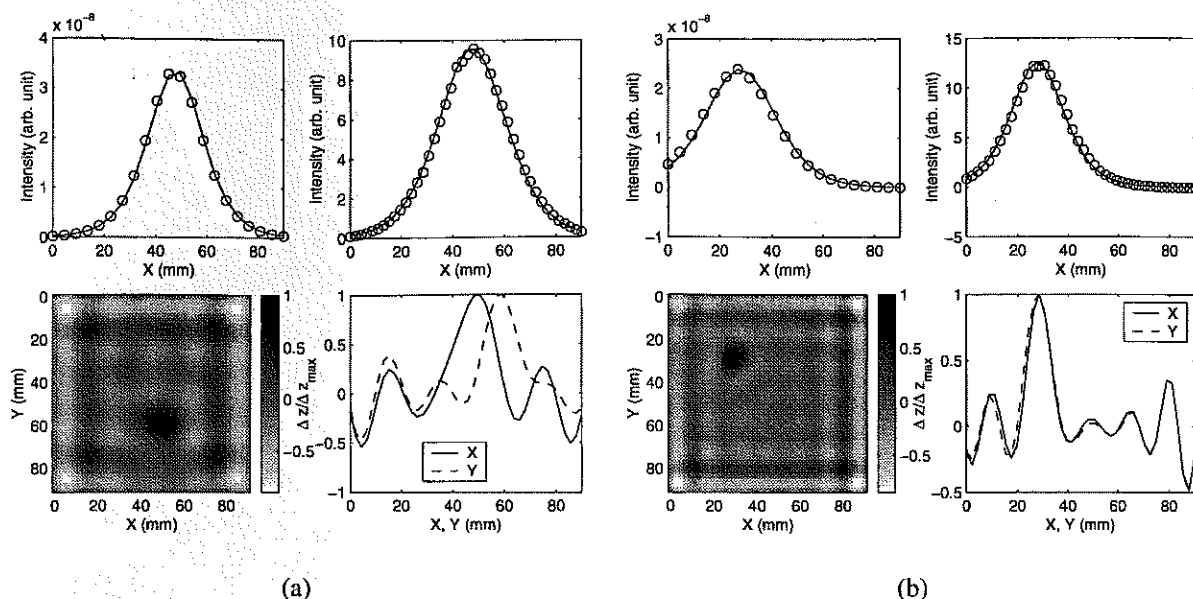
Figure 2. Fitting of the independent intensity distribution of the absorptive objects of volume $6.75 \times 6.75 \times 4.69 \text{mm}^3$ inside the slab described in the text for (a) the first absorptive object at $(50, 60, 20)$mm and (b) the second absorptive object at $(30, 30, 30)$mm. For each case, the Green's function at the source and detector planes (circle) are shown with the fitting in solid lines [the first row]. The longitudinal thickness map of the target and the thickness profiles along X and Y directions are also displayed [the second row].
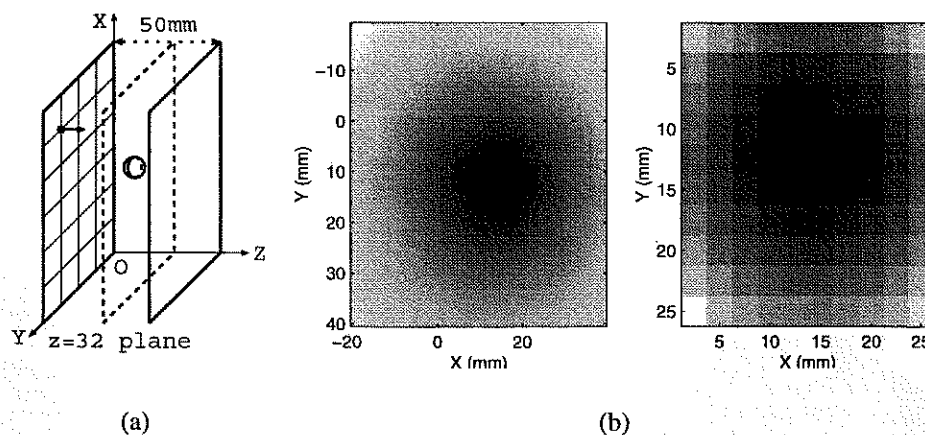

Figure 3. (a) The schematic diagram showing a fluorescent sphere embedded inside a slab. (b) Independent intensity distributions of the fluorescence from the target generated by ICA at the detector plane (Left) and at the source plane (Right). The fluorescent sphere is located on the $z = 32$mm plane.

grids. The grid spacing on the detector plane is 1.23mm.

Independent intensity distributions at the detector plane and the source plane obtained by ICA is shown in Fig. 3(b). The fluorescent target is found to be centered at $(x, y) = (11, 9)$mm and $z = 33$mm away from the input window by fitting independent intensity distributions at the detector plane and the source plane to the Green's functions in the diffusion approximation [see Fig. 4(a) and (b)]. The (x, y) coordinate agrees exactly with the known xy coordinates and the z coordinate is within 1mm error of the known z coordinate. The

Two
alized
ıd the
ıd the
file of
show

.6mm,
size of
;orptive

: 50mm
cent tar-
:ould be
wo long
ngth and
:ring and
ıre water
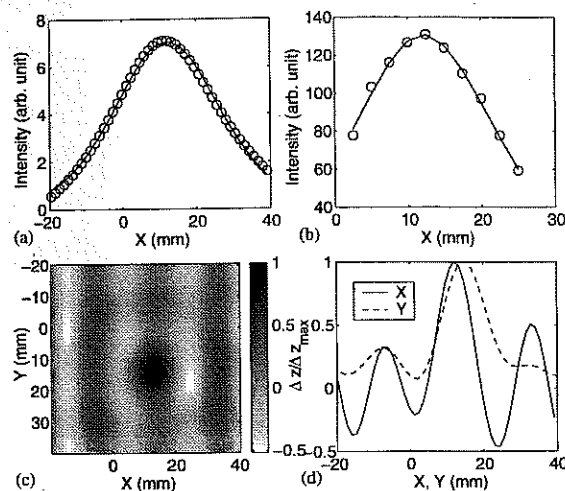'2mm^{-1}
, respec-
from the
nsecutive

Figure 4. Fitting of the independent intensity distribution of fluorescence from a sphere of diameter 9mm embedded in Intralipid-10% solution to the Green's function (a) at the detector plane and (b) at the source plane. (c) The longitudinal thickness map of the target centered at $(11,9)$mm. (d) The thickness profiles along X and Y directions.

fluorescence strength is obtained to be $f = 0.0462 \text{mm}^3/\text{ps}$.

The thickness map is back-projected using Eq. (7) and presented in Fig. 4(c). The horizontal and vertical thickness profiles of $\Delta z/\Delta z_{max}$ passing through the center are also plotted in Fig. 4(d). The target is observed to have a circular shape. The FWHM of the peak found to be $d = 11.5$mm. This value should be compared to the diameter of the fluorescent target 9mm.

ACKNOWLEDGMENTS

REFERENCES

1. A. Yodh and B. Chance, "Spectroscopy and imaging with diffusing light," *Phys. Today* **48**(3), pp. 38–40, 1995.
2. S. K. Gayen and R. R. Alfano, "Emerging optical biomedical imaging techniques," *Opt. Photon. News* **7**(3), pp. 17–22, 1996.
3. W. Cai, S. K. Gayen, M. Xu, M. Zevallos, M. Alrubaiee, M. Lax, and R. R. Alfano, "Optical tomographic image reconstruction from ultrafast time-sliced transmission measurements," *Appl. Opt.* **38**(19), pp. 4237–4246, 1999.
4. S. R. Arridge, "Optical tomography in medical imaging," *Inverse Problems* **15**, pp. R41–R93, 1999.
5. M. Xu, M. Lax, and R. R. Alfano, "Time-resolved Fourier optical diffuse tomography," *J. Opt. Soc. Am. A* **18**(7), pp. 1535–1542, 2001.
6. H. Dehghani, B. W. Pogue, S. P. Poplack, and K. D. Paulsen, "Multiwavelength three-dimensional near-infrared tomography of the breast: initial simulation, phantom, and clinical results," *Appl. Opt.* **42**, pp. 135–145, 2003.
7. W. Cai, M. Xu, and R. R. Alfano, "Three dimensional radiative transfer tomography for turbid media," *IEEE JSTQE* **9**, pp. 189–198, 2003.
8. M. S. Patterson and B. W. Pogue, "Mathematical model for time-resolved and frequency-domain fluorescence spectroscopy in biological tissues," *Appl. Opt.* **33**, pp. 1963–1974, Apr. 1994.

9. A. B. Milstein, S. Oh, K. J. Webb, C. A. Bouman, Q. an Zhang, D. A. Boas, and R. P. Millane, "Fluorescence optical diffusion tomography," *Appl. Opt.* **42**, pp. 3081–3094, June 2003.

10. A. D. Klose and A. Hielscher, "Fluorescence tomography with simulated data based on the equation of radiative transfer," *Opt. Lett.* **28**, pp. 1019–1021, June 2003.

11. A. H. Gandjbakhche, V. Chernomordik, J. C. Hebden, and R. Nossal, "Time-dependent contrast functions for quantitative imaging in time-resolved transillumination experiments," *Appl. Opt.* **37**, pp. 1973–1981, Apr. 1998.

12. D. Nuzillard and J.-M. Nuzillard, "Application of blind source separation to 1-d and 2-d nuclear magnetic resonance spectroscopy," *IEEE Signal Processing Letters* **5**(8), pp. 209–211, August 1998.

13. R. Vigário, J. Särelä, V. Jousmäki, M. Hämäläinen, and E. Oja, "Independent component approach to the analysis of EEG and MEG recordings," *IEEE Trans. Biomedical Engineering* **47**(5), pp. 589–593, 2000.

14. A. J. Bell, "Information theory, independent component analysis, and applications," in *Unsupervised Adaptive Filtering, Vol. I*, S. Haykin, ed., pp. 237–264, Wiley, 2000.

15. A. Hyvärinen, J. Karhunen, and E. Oja, *Independent Component Analysis*, John Wiley, New York, 2001. 481+xxii pages.

16. M. Xu, M. Alrubaiee, S. K. Gayen, and R. R. Alfano, "Three-dimensional localization and optical imaging of objects in turbid media using independent component analysis," *Appl. Opt.* , 2004. (accepted).

17. H. Heusmann, J. Kölzer, and G. Mitic, "Characterization of female breasts *in vivo* by time resolved and spectroscopic measurements in near infrared spectroscopy," *J. Biomed. Opt.* **1**, pp. 425–434, 1996.

d in
linal

rtical
erved
red to

R, and
MD17-
k MD
cement

5.
pp. 17–

c image
99.

A **18**(7),

-infrared
3.
E JSTQE

nce spec-